UNIVERSIDADE ESTADUAL PAULISTA - UNESP
University of São Paulo State "Júlio de Mesquita Filho" - campus de Guaratinguetá

VANESSA MARIA FRANCISCO DE MOURA

Dust transport between Saturn families

Guaratinguetá
2026

VANESSA MARIA FRANCISCO DE MOURA

Dust transport between Saturn families

Doctoral Thesis presented to the Graduate Program in Physics and Astronomy of the University of São Paulo State "Júlio de Mesquita Filho" as a partial requirement to obtain the degree of Doctor in Physics and Astronomy

Supervisor: Prof. Dr. Rafael Sfair

Guaratinguetá

2026

M929d

Moura, Vanessa Maria Francisco de

Dust transport between Saturn families / Vanessa Maria Francisco de Moura - Guaratinguetá, 2026.

84 f : il.

Bibliografia: f. 75-78

Tese (Doutorado) – Universidade Estadual Paulista, Faculdade de Engenharia e Ciências de Guaratinguetá, 2026.

Orientador: Prof. Dr. Rafael Sfair

1. Satélites. 2. Saturno (Planeta) 3. Poeira cósmica.
4. Astronomia. I. Título.

CDU 523.46(043)

Luciana Máximo
Bibliotecária/CRB-8 3595

unesp

UNIVERSIDADE ESTADUAL PAULISTA
CAMPUS DE GUARATINGUETÁ

ESTA TESE FOI JULGADA ADEQUADA PARA A OBTENÇÃO DO TÍTULO DE
“DOUTORA EM FÍSICA”

PROGRAMA: FÍSICA E ASTRONOMIA
CURSO: DOUTORADO

APROVADA EM SUA FORMA FINAL PELO PROGRAMA DE PÓS-GRADUAÇÃO

Profª Draª OLIVIA MARIA BERENGUE
Coordenadora

B A N C A   E X A M I N A D O R A:

Documento assinado digitalmente
gov.br RAFAEL SFAIR DE OLIVEIRA
Data: 03/03/2026 11:23:10-0300
Verifique em https://validar.iti.gov.br

PROF. DR. Rafael Sfair de Oliveira
Orientador / UNESP/FEG

Documento assinado digitalmente
gov.br SILVIA MARIA GIULIATTI WINTER
Data: 02/03/2026 11:46:05-0300
Verifique em https://validar.iti.gov.br

PROFA. DRA. Silvia Maria Giuliatti Winter
UNESP/FEG

Documento assinado digitalmente
gov.br DANIELA CARDOZO MOURAO
Data: 26/02/2026 15:49:11-0300
Verifique em https://validar.iti.gov.br

PROFA. DRA. Daniela Cardozo Mourão
UNESP/FEG

Documento assinado digitalmente
gov.br GUSTAVO BENEDETTI ROSSI
Data: 26/02/2026 10:33:35-0300
Verifique em https://validar.iti.gov.br

PROF. DR. Gustavo Benedetti Rossi
Linea
participou por videoconferência

Documento assinado digitalmente
gov.br ALTAIR RAMOS GOMES JUNIOR
Data: 25/02/2026 17:22:21-0300
Verifique em https://validar.iti.gov.br

PROF. DR. Altair Ramos Gomes Júnior
Universidade Federal de Uberlândia
participou por videoconferência

Fevereiro de 2026

Academic Background

Vanessa Moura

BIRTH	12/10/1996 - Guaratinguetá / SP
FILLIATION	Jefferson José Ribeiro de Moura Lidia Maria Pereira Francisco de Moura

FORMATION

2014 - 2019	Bachelor in Physics University of São Paulo State University (UNESP)
2019 - 2022	Master in Physics and Astronomy University of São Paulo State University (UNESP)
2022 - Present	Doctorate in Physics and Astronomy University of São Paulo State University (UNESP)

Dedico este trabalho a minha mãe Lidia.

Acknowledgements

I would like to express my gratitude and dedicate this dissertation to the people who, directly or indirectly, contributed to the realization of this work.

To my parents, Lidia and Jefferson, for the education they provided me, for their affection, understanding, and unconditional support from the moment I decided to study Physics until now. Without you, none of this would have been possible.

To my family, for their constant encouragement and confidence in my abilities. I am very proud to be part of this family.

To my boyfriend André Lemos, for his constant support and encouragement throughout this journey.

To my best friend and classmate Ana Luiza, who shared this dream with me since graduation.

To my friends, who have always motivated me and supported me throughout this journey, sharing both joys and challenges.

To my advisor, Prof. Dr. Rafael Sfair, whose guidance since my undergraduate studies was essential. His teachings, dedication, and supervision were fundamental to the development of this project.

To Patrícia Buzzatto, for her invaluable assistance in the development of the program that supported this work.

To CAPES, for the financial support that made this research possible.

I am deeply grateful to all of you.

This work was carried out with the support of the Coordination for the Improvement of Higher Education Personnel (CAPES), Brazil — Finance Code 001; and the São Paulo Research Foundation (FAPESP) — Grant No. 2016/24561-0.

“Remember, the journey of a thousand miles
begins with the first step“
(The Lion King)

Abstract

This work investigates the production and evolution of dust particles in Saturn's satellite system, exploring the mechanisms responsible for generating these particles and the dynamical processes that affect their trajectories. Dust particles are predominantly produced by impacts of IDPs (Interplanetary Dust Particles) on the surfaces of the satellites, resulting in the ejection of material. After being ejected, these particles are influenced by gravitational and non-gravitational forces such as solar radiation, electromagnetic forces, and plasma drag. These perturbations modify the orbital elements of the particles, and consequently they migrate through the regions associated with the Norse, Inuit, and Gallic families.

Investigating the transport of dust between Saturn's satellites is important for understanding the dynamics and evolution of the Saturnian system. Analyzing the migration of these particles makes it possible to identify patterns of material exchange between different regions, as well as to review potential connections between satellite populations. For this purpose, we developed a computational model using the IAS15 integrator from the REBOUND package (Rein & Spiegel 2015), which enables high-precision simulations of the bodies' positions and velocities over time and allows for the inclusion of non-gravitational forces. The model considers the gravitational interaction between Saturn, its satellites, and the dust particles, in addition to the effects of perturbative forces. The simulations included a set of particles distributed across different sizes and initial conditions. The particles were ejected isotropically from the surfaces of the satellites, and their trajectories were tracked until they reached sinks such as collision with the planet or ejection from the system.

This work explores the mechanisms responsible for dust transport around Saturn, with emphasis on the forces that affect particle trajectories after ejection and on the factors that determine their final fate. Our objective is to understand how these particles migrate between the satellite families and which processes govern the distribution of material. Furthermore, the methods and results presented here contribute to the development of future investigations on dust transport and evolution in other planetary systems, such as Jupiter, as well as the modeling of systems with similar characteristics.

The results obtained indicate that the orbital characteristics of dust-generating satellites directly influence the fate of ejected particles within the Saturnian system. It is observed that particles generated by satellites located closer to the planet to exhibit longer orbital stability times, as they are less affected by solar radiation pressure, even in cases of high eccentricities. In contrast, smaller particles at greater distances from Saturn experience significant perturbations from solar radiation, while gravitational and electromagnetic effects dominate in regions closer to the planet.

Keywords: dust particle, Saturn satellites, perturbative forces, migration, families.

List of Figures

List of Tables

Contents

Chapter 1

Introduction

The Saturnian system, composed of 274 moons (as of 2024) and a complex ring system, constitutes a favorable environment for the study of dynamical processes and physical interactions. Among the most relevant phenomena are the production and evolution of dust particles, which are fundamental to maintaining the structures observed around the planet, including the rings and the regions adjacent to the satellites.

Dust particles are generated primarily by impacts of IDPs (Interplanetary Dust Particles) on the surfaces of the satellites (Poppe 2016), resulting in the ejection of material. From the moment they are launched, these particles are subjected to perturbative forces, such as planetary oblateness, electromagnetic forces, solar radiation, and plasma drag. These forces act simultaneously, shaping the trajectories of the particles and influencing their distribution and lifetimes.

Numerous studies have documented the presence and motion of dust particles in planetary systems. Examples include the dust clouds generated by impacts on Jupiter's Galilean satellites (Sremčević et al. 2005), the formation of Saturn's G ring from particles originating in Aegaeon (Madeira et al. 2018), dust fluxes in the outer Solar System (Poppe 2016), and the study of Mab as a source of Uranus's μ ring (Sfair & Giuliatti Winter 2012).

The goal of this work is to understand how particles migrate among Saturn's satellite families, analyzing their trajectories from the moment of ejection to their final fate. The results obtained here provide important perspectives on the dynamics that shape dust distributions in planetary systems.

We develop a computational model to simulate the production and evolution of dust particles in the Saturnian system, considering the main forces acting on them. We use the IAS15 integrator from the REBOUND package (Rein & Spiegel 2015), which allows for the inclusion of non-gravitational forces and enables high-precision simulations. This model allows us to explore the dynamics of particles ejected from the satellites, following their trajectories from ejection to their sinks, such as collisions or escape from the system.

This thesis is structured into six main chapters. Chapter 1 presents the context, motivation, and objectives of the study, along with its scientific relevance. Chapter 2 details the general characteristics of the planet and its satellites, including their division into families and the factors that influence dust production. In Chapter 3, we discuss the perturbative forces acting on dust particles and the methods used to compute dust-production rates. Chapter 4 describes the computational model developed, the initial conditions, and the approaches used in the simulations. In Chapter 5, we analyze the effects of perturbative forces and the inclusion of satellites on the particles' orbital evolution, as well as their dynamical behavior when associated with each dynamical family. Additionally, we present an analysis of the particle migration process among the different families of the Saturnian system. Finally, Chapter 6 discusses the main results of the study, its limitations, and future steps.

Chapter 2

Saturn system

Currently, Saturn is the planet with the largest number of known natural satellites in the Solar System, with 274 confirmed moons as of 2024. These satellites are commonly classified into two main categories: regular and irregular satellites. Regular satellites typically orbit close to the planet, following nearly circular and low-inclination orbits, and are believed to have formed within the circumplanetary disk during the early stages of the planet's formation. In contrast, irregular satellites orbit at much larger distances and generally exhibit highly inclined and eccentric orbits, suggesting that they were captured by the planet's gravitational field during the early evolution of the Solar System (Nesvorný et al. (2003); Sheppard & Jewitt (2003)).

The group of larger satellites, listed in Table A.3, consists of regular bodies with radii greater than 100 km. In contrast, the irregular satellites are typically classified based on similarities in their semi-major axis, eccentricity, and inclination, which suggest common dynamical origins. Because several of these objects share similar orbital characteristics, they are organized into dynamical families, as illustrated in Figure 2.1. The orbital ranges used to define these groups are summarized in Table 2.1.

Table 2.1: Orbital parameters of the irregular satellite groups of Saturn.

Group	**a (R_S)**	**I (deg)**	**e**
Norse	198.91 – 430.96	100 – 177	0.13 – 0.77
Inuit	182.33 – 298.36	25 – 80	0.15 – 0.48
Gallic	265.20 – 314.93	10 – 50	0.53

The identification of these dynamical families suggests that many irregular satellites may have originated from the collisional fragmentation of larger progenitor bodies after their capture by Saturn (Nesvorný et al. 2007). Based on their orbital characteristics, the irregular satellites of Saturn are generally divided into three main groups: the Inuit, Gallic, and Norse families.

The Inuit family is composed of satellites with prograde orbits and moderate inclinations. Some of the most prominent members of this group include Siarnaq, Paaliaq, Kiviuq, and Ijiraq. These objects orbit Saturn at distances of roughly 11–19 million kilometers and share similar orbital and photometric properties, suggesting a common collisional origin.

The Gallic family also contains prograde satellites, but with slightly different orbital inclinations and semi-major axes. The main members of this group are Albiorix, Tarvos, and Erriapus. Among them, Albiorix is the largest and is often considered the possible progenitor body of the group (Gladman et al. (2001); Nesvorný et al. (2007)).

The Norse family represents the largest population of irregular satellites around Saturn and is characterized by retrograde orbits, with high inclinations and a wide range of eccentricities. Members of this group include Ymir, Skathi, Surtur, and Fenrir. The large dispersion in their orbital elements suggests that this group may contain multiple subfamilies produced by different collisional events (Nesvorný et al. (2003); Nesvorný et al. (2007)).

The number of known satellites of Saturn has increased significantly in recent years due to improvements in observational surveys. Until 2019, 62 satellites of Saturn had been confirmed. In 2019, a team from the Carnegie Institution for Science in Washington, led by Scott S. Sheppard, announced the discovery of 20 moons, making Saturn the planet with the largest number of known satellites at the time (Greshko 2019). These moons, with radii smaller than 5 km, included 17 objects on retrograde orbits and 3 on prograde orbits, as detailed in Table A.4. They were discovered through observations conducted between 2004 and 2007 using the Subaru Telescope, located at the top of the Mauna Kea volcano in Hawaii.

Later, in 2023, a research team led by Edward Ashton from Academia Sinica used data from the Canada–France–Hawaii Telescope to analyze sequential images obtained between 2019 and 2021 (Persan 2023). This analysis resulted in the confirmation of 62 additional satellites orbiting Saturn (Table A.5).

More recently, in 2025, the same research group led by Edward Ashton reported the discovery of 128 additional moons, also using observations from the Canada–France–Hawaii Telescope obtained in 2023. This discovery increased the total number of confirmed satellites orbiting Saturn to 274 (Ashton et al. 2025).

In Figure 2.1, the regions corresponding to Saturn's dynamical families are illustrated. The values used to generate the plot were extracted from the data employed in the simulations, as presented in Tables A.1 to A.5. The Norse group is shown in blue, the Inuit family in red, and the Gallic group in green. Closer to the planet, the region occupied by the larger satellites is indicated in purple. The horizontal dotted line marks an inclination of 90 degrees, contrasting the satellites by their orbital motion: objects above this line follow retrograde

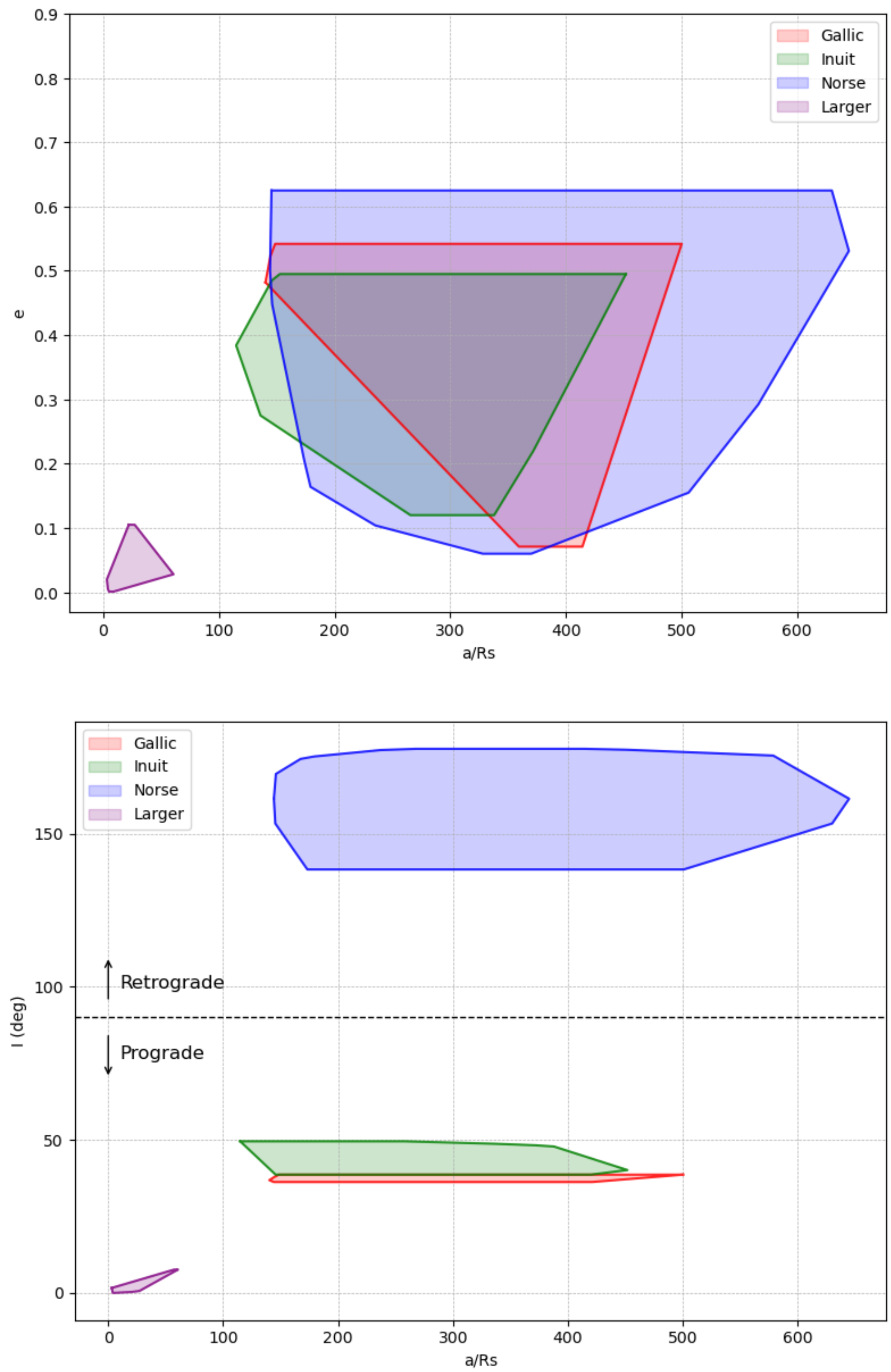

Figure 2.1: Distribution of Saturn's satellites by dynamical groups. The satellites of the Norse group are shown in blue, those of the Inuit group in green, and those of the Gallic group in red. The larger and inner satellites are highlighted in purple. The regions were defined based on the periapsis and apoapsis values of each satellite.

orbits, moving opposite to Saturn's rotation, whereas those below exhibit prograde motion, orbiting in the same direction as the planet's rotation.

2.0.1 Albiorix

Albiorix is an irregular satellite of Saturn that is part of the Gallic group of satellites. It was discovered in 2000 by a team led by Brett J. Gladman. Albiorix has a prograde orbit that is highly inclined and eccentric with respect to the planet's equatorial plane, characteristics typical of irregular satellites, which were likely captured gravitationally by Saturn during the early stages of the Solar System's formation.

This satellite has an estimated diameter of approximately 30 km and orbits Saturn at an average distance of about 16 million kilometers. Albiorix is considered the largest member of the Gallic group, which also includes the satellites Tarvos and Erriapus. Studies suggest that these satellites may have originated from the fragmentation of a larger progenitor body, possibly Albiorix itself, following a collisional event.

Due to its orbital properties and its possible origin as the progenitor body of the Gallic group, Albiorix is an object of interest for studies on the dynamics and evolution of Saturn's irregular satellite populations.

2.0.2 Phoebe

Phoebe is an irregular satellite of Saturn, discovered in 1899 by the astronomer William Henry Pickering. In contrast to most of the planet's satellites, Phoebe has a retrograde orbit that is highly inclined and eccentric, characteristics typical of objects that were gravitationally captured.

With a mean diameter of approximately 213 km, Phoebe is one of the largest irregular satellites of Saturn and orbits the planet at an average distance of about 13 million kilometers. Detailed observations performed by the Cassini–Huygens spacecraft during a flyby in 2004 revealed a heavily cratered surface composed of a mixture of ice and dark rocky material.

Due to its physical and orbital properties, Phoebe is believed to have originated in the outer regions of the Solar System, possibly in the Kuiper Belt, and was later captured by Saturn's gravity. In addition, studies indicate that material ejected from Phoebe's surface may contribute to the formation of the extensive Phoebe ring, a diffuse ring of dust that extends around the planet.

2.0.3 Rhea

Rhea is the second-largest satellite of Saturn and was discovered in 1672 by the astronomer Giovanni Domenico Cassini. With a mean diameter of approximately 1,528 km, Rhea is composed mainly of water ice, with a small fraction of rocky material, which gives it a relatively low density.

Rhea's surface is heavily cratered, indicating a long geological history with limited recent internal activity. Observations performed by the Cassini–Huygens mission also revealed the presence of large systems of fractures and faults, as well as a surface dominated by bright ice.

Rhea orbits Saturn at an average distance of approximately 527,000 kilometers and has an orbital period of about 4.5 days. Studies also suggest that the satellite may be surrounded by an extremely tenuous system of dust rings, although this hypothesis is still under investigation.

2.0.4 Siarnaq

Siarnaq is an irregular satellite of Saturn that is part of the Inuit group of satellites. It was discovered in 2000 by a team of astronomers led by Brett J. Gladman during observations made with ground-based telescopes.

Siarnaq has a prograde orbit that is relatively inclined and eccentric around Saturn, characteristics commonly observed among the planet's irregular satellites. The satellite has an estimated diameter of approximately 40 km, and is one of the largest members of the Inuit group, and it orbits Saturn at an average distance of about 17 million kilometers.

Due to the orbital similarities among the members of this group, it is believed that Siarnaq and other associated satellites may have originated from the fragmentation of a larger progenitor body following a collisional event. The study of these satellites contributes to the understanding of the origin and dynamical evolution of Saturn's irregular satellite populations.

2.0.5 Ymir

Ymir is an irregular satellite of Saturn that is part of the Norse group of satellites. It was discovered in 2000 by a team led by Brett J. Gladman during observations made with ground-based telescopes.

Ymir has a retrograde orbit that is highly inclined and eccentric around Saturn, characteristics typical of the planet's irregular satellites. The satellite has an estimated diameter of approximately 18 km and orbits Saturn at an average distance of about 23 million kilometers, with an orbital period of approximately four Earth years.

Like other members of the Norse group, Ymir is believed to be an object that was gravitationally captured by Saturn during the early stages of the Solar System's formation.

Chapter 3

Model dynamics

Dust particles in the Saturnian system are continuously generated by hypervelocity impacts of interplanetary dust particles (IDPs) on the surfaces of the irregular satellites. Once ejected, these grains are subsequently subject to the action of a variety of gravitational and non-gravitational forces that modify their orbital elements and transport them throughout the system.

The motion of a dust particle is governed by the superposition of all relevant accelerations, which we write in the form:

$$\ddot{\vec{r}} = \ddot{\vec{r}}_{G_S} + \ddot{\vec{r}}_L + \ddot{\vec{r}}_{RP} + \ddot{\vec{r}}_{PR} + \ddot{\vec{r}}_{PD} + \ddot{\vec{r}}_{G_{sat}}, \tag{3.1}$$

where the terms on the right-hand side correspond, respectively, to the gravitational field of Saturn (including its oblateness) ($\ddot{\vec{r}}_{G_S}$), electromagnetic forces ($\ddot{\vec{r}}_L$), solar radiation pressure ($\ddot{\vec{r}}_{RP}$), Poynting–Robertson drag ($\ddot{\vec{r}}_{PR}$), plasma drag ($\ddot{\vec{r}}_{PD}$), and the gravitational perturbations from the irregular satellites ($\ddot{\vec{r}}_{G_{sat}}$).

The numerical integrations are performed in a Saturn-centered inertial reference frame aligned with the planet's equatorial plane at the J2000 epoch. In this frame, the z-axis is defined by Saturn's spin axis, and the x and y axis completes an orthogonal right-handed frame. Forces that depend on the planet's orientation, such as those associated with the zonal harmonics or magnetically induced interactions, are evaluated using a body-fixed frame, where z_{bod} coincides with the rotation axis of Saturn and x_{bod} is aligned with the prime meridian. All physical quantities employed in the integration are expressed in the CGS unit system.

The contributions of each force listed above, as well as their physical formulation and numerical implementation, are discussed in detail in Section 3.1.

3.1 Pertubative forces

This section presents the main perturbative forces considered in our simulations and their contribution to the dynamical evolution of the particles. In addition to the dominant gravitational attraction of the central planet, small bodies in circumplanetary environments are subject to a variety of perturbations that can significantly alter their trajectories over time. These effects may lead to changes in orbital elements, influencing both the short-term dynamics and the long-term stability of the system. In the following subsections, we describe each perturbative contribution in detail, beginning with the effect of the planet's oblateness.

3.1.1 Oblateness forces

A satellite orbiting a planet is subject to several forces, with those of gravitational origin being the most predominant. When we assume a planet with a perfectly spherical and homogeneous shape, the resulting orbit is an ellipse. However, in the case of Saturn, the most oblate planet in the Solar System, its oblateness causes a deformation of this ellipse. In this section, we analyze how Saturn's planetary oblateness affects the orbits of the bodies in its system over time. This investigation will allow us to incorporate this perturbation into our code. We will follow the reasoning developed in Kuga et al. (2011).

Considering two points $P(r, \theta, \lambda)$ and $P'(r', \theta', \lambda')$, as shown in Figure 3.1, r is the distance from the origin, θ is the colatitude, and λ is the longitude.

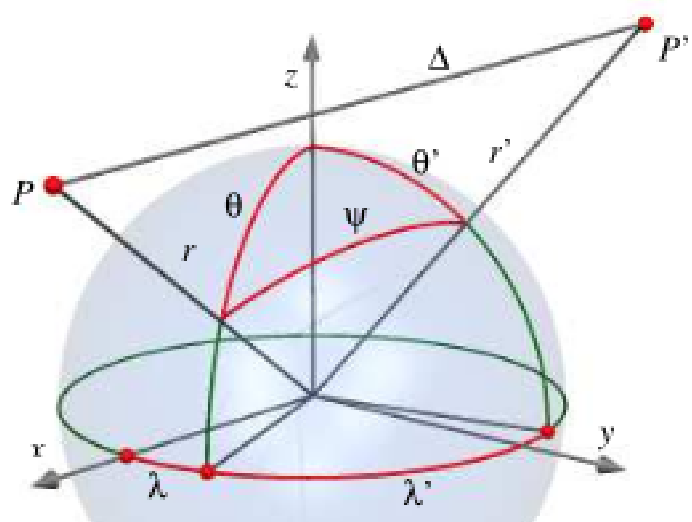

Figure 3.1: Illustration of the position of the particle $P(r, \theta, \lambda)$ and the mass element $P'(r', \theta', \lambda')$ with respect to the planet's center of mass. Source: Kuga et al. (2011)

We begin with the expression for the potential of a mass element dM:

$$U_{dM} = \frac{GM}{r} \sum_{n=0}^{\infty} \left(\frac{r'}{r}\right)^n P_n(\cos\Psi) \tag{3.2}$$

where Ψ is the angle between the position vectors of P and P'.

Applying Legendre's addition theorem, we obtain:

$$P_n(\cos\Psi) = \sum_{m=0}^{n} (2-\delta_{mn}) \frac{(n-m)!}{(n+m)!} P_n^m(\cos\theta) P_n^m(\cos\theta') \cos m(\lambda-\lambda') \tag{3.3}$$

Considering the complementary angles φ and φ' of θ and θ', the potential can be rewritten as:

$$U_{dM} = \frac{GM}{r} \sum_{n=0}^{\infty} \sum_{m=0}^{n} (2-\delta_{nm}) \frac{(n-m)!}{(n+m)!} \left(\frac{r'}{r}\right)^n P_n^m(\sin\varphi) P_n^m(\sin\varphi') \cos m(\lambda-\lambda') \tag{3.4}$$

where G is the universal gravitational constant, δ_{mn} is the Kronecker delta, and P_n^m are the associated Legendre polynomials.

The integration over the entire mass distribution provides the potential (Kuga et al. 2011):

$$U = \frac{GM}{r} \sum_{n=m}^{\infty} \sum_{m=0}^{n} \left(\frac{a_e}{r}\right)^n (C_{nm}\cos m\lambda + S_{nm}\sin m\lambda) P_n^m(\sin\varphi) \tag{3.5}$$

with spherical harmonic coefficients C_{nm} and S_{nm} are defined as:

$$\begin{bmatrix} C_{nm} \\ S_{nm} \end{bmatrix} = \frac{(2-\delta_{m0})}{a_e^n M} \frac{(n-m)!}{(n+m)!} \int_M r'_n P_n^m(\sin\varphi') \begin{bmatrix} \cos m\lambda' \\ \sin m\lambda \end{bmatrix} dM \tag{3.6}$$

where a_e is the equatorial semi-major axis of the planet's ellipsoid, and M is its mass.

The potential of a spheroid, expanded up to terms of sixth order, can be written as:

$$U = \frac{GM_p}{r}\left[1 - \sum_{n=2}^{6} J_n \left(\frac{R_p}{r}\right)^n P_n(\sin\varphi)\right] \tag{3.7}$$

$$= \frac{GM_p}{r}\left[1 - J_2 \left(\frac{R_p}{r}\right)^2 P_2(\sin\varphi) - J_4 \left(\frac{R_p}{r}\right)^4 P_4(\sin\varphi) - J_6 \left(\frac{R_p}{r}\right)^6 P_6(\sin\varphi)\right] \tag{3.8}$$

with J_n representing the zonal harmonics and P_n the Legendre polynomials. In this work, we use only even–degree harmonics, since we are interested in the coefficients that are symmetric with respect to the equatorial plane.

From the potential, we compute the forces associated with the J_2, J_4, and J_6 harmonics, which are essential for modeling the effects of planetary oblateness on the orbits of the satellites:

$$\vec{F}_{J_2} = -GM_p\nabla\left[\frac{1}{r}\left(1 - J_2\left(\frac{R_p}{r}\right)^2 P_2(\sin\varphi)\right)\right] \tag{3.9}$$

$$\vec{F}_{J_4} = -GM_p\nabla\left[\frac{1}{r}\left(-J_4\left(\frac{R_p}{r}\right)^4 P_4(\sin\varphi)\right)\right] \tag{3.10}$$

$$\vec{F}_{J_6} = -GM_p\nabla\left[\frac{1}{r}\left(-J_6\left(\frac{R_p}{r}\right)^6 P_6(\sin\varphi)\right)\right] \tag{3.11}$$

Using the following Legendre polynomials:

$$P_2(\sin\varphi) = \frac{1}{2}(3(\sin\varphi)^2 - 1) \tag{3.12}$$

$$P_4(\sin\varphi) = \frac{1}{8}(35(\sin\varphi)^4 - 30(\sin\varphi)^2 + 3) \tag{3.13}$$

$$P_6(\sin\varphi) = \frac{1}{16}(231(\sin\varphi)^6 - 315(\sin\varphi)^4 + 105(\sin\varphi)^2 - 5) \tag{3.14}$$

We obtain the x, y, and z components of the force for the J_2 coefficient:

$$F_{xJ_2} = -\frac{GM_p}{r^3}\left[1 + \frac{3}{2}J_2\left(\frac{R_p}{r}\right)^2 - \frac{15}{2}J_2\frac{R_p^2}{r^4}z^2\right]x \tag{3.15}$$

$$F_{yJ_2} = -\frac{GM_p}{r^3}\left[1 + \frac{3}{2}J_2\left(\frac{R_p}{r}\right)^2 - \frac{15}{2}J_2\frac{R_p^2}{r^4}z^2\right]y \tag{3.16}$$

$$F_{zJ_2} = -\frac{GM_p}{r^3}\left[1 + \frac{9}{2}J_2\left(\frac{R_p}{r}\right)^2 - \frac{15}{2}J_2\frac{R_p^2}{r^4}z^2\right]z \tag{3.17}$$

Similarly, for the J_4 coefficient:

$$F_{xJ_4} = -\frac{GM_p}{r^3}\left[-\frac{15}{8}J_4\left(\frac{R_p}{r}\right)^4 + \frac{210}{8}J_4\frac{R_p^4}{r^6}z^2 - \frac{315}{8}J_4\frac{R_p^4}{r^8}z^4\right]x \tag{3.18}$$

$$F_{yJ_4} = -\frac{GM_p}{r^3}\left[-\frac{15}{8}J_4\left(\frac{R_p}{r}\right)^4 + \frac{210}{8}J_4\frac{R_p^4}{r^6}z^2 - \frac{315}{8}J_4\frac{R_p^4}{r^8}z^4\right]y \tag{3.19}$$

$$F_{zJ_4} = -\frac{GM_p}{r^3}\left[-\frac{75}{8}J_4\left(\frac{R_p}{r}\right)^4 + \frac{350}{8}J_4\frac{R_p^4}{r^6}z^2 - \frac{315}{8}J_4\frac{R_p^4}{r^8}z^4\right]z \tag{3.20}$$

And for the J_6 coefficient:

$$F_{xJ_6} = -\frac{GM_p}{r^3}\left[-\frac{105}{16}J_6\left(\frac{R_p}{r}\right)^6 + \left(\frac{1}{3} + 9\left(\frac{z}{r}\right)^2 - 33\left(\frac{z}{r}\right)^4 + \frac{143}{5}\left(\frac{z}{r}\right)^6\right)\right]x \tag{3.21}$$

$$F_{yJ_6} = -\frac{GM_p}{r^3}\left[-\frac{105}{16}J_6\left(\frac{R_p}{r}\right)^6 + \left(\frac{1}{3} + 9\left(\frac{z}{r}\right)^2 - 33\left(\frac{z}{r}\right)^4 + \frac{143}{5}\left(\frac{z}{r}\right)^6\right)\right]y \tag{3.22}$$

$$F_{zJ_6} = -\frac{GM_p}{r^3}\left[-\frac{105}{16}J_6\left(\frac{R_p}{r}\right)^6 + \left(\frac{7}{3} + 21\left(\frac{z}{r}\right)^2 - \frac{231}{5}\left(\frac{z}{r}\right)^4 + \frac{143}{5}\left(\frac{z}{r}\right)^6\right)\right]z \tag{3.23}$$

where M_p is the mass of the planet, r is the distance between the two bodies, J_2, J_4, and J_6 are the dimensionless coefficients associated with the planet's oblateness, and (x, y, z) are the coordinates of the particle with respect to the center of mass.

To derive the equations describing the variation of the orbital elements of a particle orbiting an oblate body, we start from Lagrange's planetary equations and introduce the disturbing function associated with planetary oblateness, considering only the quadrupole term J_2.

$$\left\langle \frac{da}{dt} \right\rangle_{J_2} = 0, \tag{3.24}$$

$$\left\langle \frac{de}{dt} \right\rangle_{J_2} = 0, \tag{3.25}$$

$$\left\langle \frac{dI}{dt} \right\rangle_{J_2} = 0, \tag{3.26}$$

$$\left\langle \frac{d\Omega}{dt} \right\rangle_{J_2} = -\frac{3nJ_2R_p^2}{2a^2(1-e^2)^2}\cos I, \tag{3.27}$$

$$\left\langle \frac{d\omega}{dt} \right\rangle_{J_2} = \frac{3nJ_2R_p^2}{2a^2(1-e^2)^2}\left(2-\frac{5}{2}\sin^2 I\right), \tag{3.28}$$

$$\left\langle \frac{dM}{dt} - n \right\rangle_{J_2} = \frac{3nJ_2R_p^2}{2a^2(1-e^2)^{3/2}}\left(1-\frac{3}{2}\sin^2 I\right). \tag{3.29}$$

The terms on the right-hand side of Eq. 3.29 should, in principle, be placed within brackets, since the short-period variations have been neglected. However, we omit this notation here and in the following equations, and consider only the mean variation.

The first three equations (3.24-3.26) indicate that the elements a, e, and I remain constant; therefore, planetary oblateness does not affect these orbital elements in the averaged sense. As a consequence, the right-hand sides of the last three equations (3.27-3.29) become fixed. The angles ω and Ω will circulate with values that vary linearly in time. Since their circulation periods are approximately $(a/R_p)^2/J_2$ times longer than the orbital period, the solution of Eq. 3.29 corresponds to a slowly rotating ellipse. For the case of polar orbits ($I = 0°$), the ascending node (Ω) does not precess.

For polar orbits, the precession of the pericenter is slower, while for equatorial orbits ($I = 90°$), the pericenter precesses more quickly.

The last equation 3.29 describes the mean rate at which a particle completes an orbit. This rate differs from the Keplerian mean motion due to the change in the particle's average angular velocity and the slow variation of the pericenter. For equatorial orbits, the term on the right-hand side of the equation is positive, causing the particle to complete its orbit more quickly than it would in an unperturbed Keplerian two-body motion.

3.1.2 Electromagnetic force

In this section, we investigate the impact of the electromagnetic force on the orbit of dust particles around a planet.

When a charged dust grain orbits in the magnetic field of a planet, it is subject to the

Lorentz force. In a rotating frame of reference near the planet, the magnetic field $\vec{B}$ rotates with an angular velocity Ω_p, and the Lorentz force can be expressed as follows, as described in Burns et al. (2001):

$$\vec{F}_{EM} = \frac{q}{c}(\vec{v}_{rel} \times \vec{B}) \tag{3.30}$$

where q represents the charge of the grain, c is the speed of light, and $\vec{v}_{rel}$ is the velocity relative to the magnetic field, defined as:

$$\vec{v}_{rel} = \vec{v} - (\vec{\Omega}_p \times \vec{r}) \tag{3.31}$$

where $\vec{v}$ is the velocity of the particle relative to an inertial frame of reference and $\vec{r}$ is the position of the grain relative to the planet.

Substituting $\vec{v}_{rel}$ into the equation (3.30), the Lorentz force becomes:

$$\vec{F}_{EM} = \frac{q}{c}([\vec{v} - (\vec{\Omega}_p \times \vec{r})] \times \vec{B}) \tag{3.32}$$

Saturn's magnetic field can be described by the potential Dougherty et al. (2018):

$$\Phi_{mag} = R_p \sum_{n=1}^{\infty} \sum_{m=0}^{n} \left(\frac{R_p}{r}\right)^{n+1} [g_n^m \cos(m\phi_R) + h_n^m \sin(m\phi_R)] P_n^m(\cos\theta) \tag{3.33}$$

where g_n^m and h_n^m are the Gauss coefficients of Saturn's magnetic field, and n and m denote the spherical harmonic degree and order, respectively. The functions $P_n^m(x)$ correspond to the associated Legendre functions. Here, ϕ_R denotes the azimuthal coordinate in the rotating reference frame, defined as $\phi_R = \phi - \Omega_p t$, where Ω_p is the planetary rotation rate. The angles ϕ and θ are the spherical coordinates in the inertial reference frame.

Different formulations can be used to describe the charge-to-mass ratio q/m_g, depending on the adopted unit system. In this work, we adopt the grain surface potential, expressed in volts, to characterize the grain charge, following and , as it exhibits only a weak dependence on particle size. Within this framework, we define the parameter $\beta_L = q/m_g c$, which relates the grain charge q to its mass m_g, scaled by the speed of light c. For spherical particles with radius b and density ρ, assuming a constant surface potential V, this parameter can be written in cgs units as $\beta_L = 2.6 \times 10^{-14} \frac{V}{b^2\rho}$, where V is given in volts.

Considering a current-free magnetic field, Maxwell's equation ($\nabla \cdot \vec{B} = \vec{0}$) allows the magnetic field to be defined as:

$$\vec{B} = -\nabla\Phi_{mag} \tag{3.34}$$

Thus, the components of Saturn's internal magnetic field can be expressed as follows: (Dougherty et al. 2018)

$$B_r = \sum_{n=1}^{\infty}\sum_{m=0}^{n}(n+1)\left(\frac{R_p}{r}\right)^{n+2}[g_m^m\cos(m\phi) + h_m^m\sin(m\phi)]P_n^m(\cos\theta) \tag{3.35}$$

$$B_\theta = -\sum_{n=1}^{\infty}\sum_{m=0}^{n}\left(\frac{R_p}{r}\right)^{n+2}[g_m^m\cos(m\phi) + h_m^m\sin(m\phi)]\frac{dP_n^m(\cos\theta)}{d\theta} \tag{3.36}$$

$$B_\phi = \sum_{n=1}^{\infty}\sum_{m=0}^{n}\left(\frac{R_p}{r}\right)^{n+2}\frac{m}{\sin\theta}[g_m^m\cos(m\phi) + h_m^m\sin(m\phi)]P_n^m(\cos\theta) \tag{3.37}$$

From equation (3.37), we see that the azimuthal component B_ϕ will only exist when the magnetic field exhibits axial asymmetry ($m \neq 0$).

We can combine the dimensionless parameters employed in the calculation to derive a relation between the electromagnetic force and the gravitational force. For a static grain ($\vec{v} = 0$) located in the equatorial plane ($\theta = 90°$), this coefficient is independent of velocity and is given by:

$$L = \frac{F_{EM}}{F_G} = \frac{qg_{1,0}R_p^3\Omega_p}{cGM_pm_g} \tag{3.38}$$

where L depends only on the properties of the grain (charge-to-mass ratio) and of the environment (planetary mass and radius, rotation rate, and dipole strength).

The magnetic field can be described by magnetic monopoles, dipoles, quadrupoles, or octupoles. The choice of which terms to include depends on the context of the study. In this work, both dipole and quadrupole contributions were initially tested; however, only the dipole term was considered in the simulations, as the inclusion of the quadrupole component did not produce significant variations in the results..

3.1.3 Dipole and quadrupole terms

For both cases, we analyze situations in which the expansion of the magnetic potential describes axial symmetry, that is, $m = 0$. In addition, we assume that the planetary angular velocity is $\vec{\Omega} = \Omega\hat{z}$.

In the case of the aligned dipole, the magnetic field is produced by the coefficient $g_{1,0}$. This dipole is aligned with the body's rotation axis, and the components of the magnetic field in spherical coordinates are given by the following expressions from Hamilton (1993):

$$B_r = 2g_{1,0}\left(\frac{R_p}{r}\right)^3 \cos\theta \tag{3.39}$$

$$B_\theta = g_{1,0}\left(\frac{R_p}{r}\right)^3 \sin\theta \tag{3.40}$$

$$B_\phi = 0 \tag{3.41}$$

Transforming the magnetic-field components (equations 3.39–3.41) into Cartesian coordinates and substituting them into the Lorentz force equation (3.30), we obtain the Cartesian components of the force for the dipole:

$$F_x = \left(\frac{q}{c}\right)[(\dot{y_g} - x_g\Omega_p)B_z - \dot{z}_g B_y] \tag{3.42}$$

$$F_y = \left(\frac{q}{c}\right)[(\dot{x_g} - y_g\Omega_p)B_z - \dot{z}_g B_x] \tag{3.43}$$

$$F_z = \left(\frac{q}{c}\right)[(\dot{x_g} - y_g\Omega_p)B_y - (\dot{y_g} - x_g\Omega_p)B_y] \tag{3.44}$$

where $\dot{x}_g$, $\dot{y}_g$ and $\dot{z}_g$ denote the components of the particle's velocity. These equations were implemented in the `REBOUND` code following the approach of Siqueira (2019).

By substituting its components (Eqs.3.39–3.41) into the Lagrange equations and performing the time averaging, we obtain the rates of change of the orbital elements for particles under the influence of the electromagnetic force for the dipole:

$$\left\langle \frac{da}{dt} \right\rangle_{g_{1,0}} = 0, \tag{3.45}$$

$$\left\langle \frac{de}{dt} \right\rangle_{g_{1,0}} = -\frac{nL}{4} e(1-e^2)^{1/2} \sin^2 I \sin 2\omega, \tag{3.46}$$

$$\left\langle \frac{dI}{dt} \right\rangle_{g_{1,0}} = \frac{nL}{4(1-e^2)^{1/2}} e^2 \sin^2 I \cos I \sin 2\omega, \tag{3.47}$$

$$\left\langle \frac{d\Omega}{dt} \right\rangle_{g_{1,0}} = \frac{nL}{(1-e^2)^{1/2}} \left[\cos I - \frac{1}{(1-e^2)} \left(\frac{n}{\Omega_p} \right) \right], \tag{3.48}$$

$$\left\langle \frac{d\omega}{dt} \right\rangle_{g_{1,0}} = \frac{nL}{(1-e^2)^{1/2}} \left[-\cos^2 I + \frac{3\cos I}{(1-e^2)} \left(\frac{n}{\Omega_p} \right) \right], \tag{3.49}$$

$$\left\langle \frac{dM}{dt} - n \right\rangle_{g_{1,0}} = -2nL, \tag{3.50}$$

For the aligned dipole, there is no variation in the semi-major axis of the particles. In the case of planar orbits ($I = 0$), the eccentricity and inclination remain constant, resulting in linear variations in the argument of pericenter and in the longitude of the ascending node, since these elements depend directly on eccentricity and inclination. However, for low inclinations and eccentricities, the electromagnetic force induces precessions in the pericenter and in the ascending node, for which rates depend on the semi-major axis, eccentricity, and inclination of the orbit.

In the case of the aligned quadrupole, the magnetic field is generated by the coefficient $g_{2,0}$. Under low-inclination conditions, the contribution from the quadrupole is negligible in comparison with that of the dipole. However, the radial component of the magnetic field has a relevant influence. For low-inclination orbits, the field generates a normal force that affects the inclination, the ascending node, and the pericenter of the particle (Hamilton 1993).

$$B_r = \frac{3}{2} g_{2,0} \left(\frac{R_p}{r} \right)^4 (3\cos^2\theta - 1) \tag{3.51}$$

The same procedure used to obtain Eqs.3.42–3.44 is applied using the quadrupole expression (Eq.3.51), allowing us to determine the force components for the quadrupole. These equations were implemented in the `REBOUND` code following the approach of Siqueira (2019).

By substituting Eq.3.51 into the planetary perturbation equations, we obtain the variations corresponding to the quadrupole case (Hamilton 1993):

$$\left\langle \frac{dI}{dt} \right\rangle_{g_{2,0}} \approx \frac{3}{2} n L \left(\frac{g_{2,0}}{g_{1,0}} \right) \left(\frac{R_p}{a} \right) \left(\frac{n}{\Omega_p} \right) \left(\frac{e \cos \omega}{(1-e^2)^{5/2}} \right), \tag{3.52}$$

$$\left\langle \frac{d\Omega}{dt} \right\rangle_{g_{2,0}} \approx \frac{\tan \omega}{\sin I} \left\langle \frac{dI}{dt} \right\rangle_{g_{2,0}}, \tag{3.53}$$

$$\left\langle \frac{d\omega}{dt} \right\rangle_{g_{2,0}} \approx - \cos I \left\langle \frac{d\Omega}{dt} \right\rangle_{g_{2,0}} \tag{3.54}$$

These expressions (3.52 to 3.54) show that the evolution of the angular orbital elements is coupled, with the inclination driving the variations in both the longitude of the ascending node and the argument of pericenter.

3.1.4 Solar Radiation

In this section, we analyze the influence of solar radiation on particles, considering the equations that describe the radiation pressure and Poynting-Robertson drag forces.

For a particle of radius r_g and density ρ, situated at a distance R from the Sun, the gravitational (F_G) and radiation pressure (F_{RP}) forces are defined as (Mignard 1984):

$$F_G = GM_\odot \frac{4}{3} \frac{\pi r_g^3 \rho}{R^2} \tag{3.55}$$

$$F_{RP} = \frac{\Phi \pi r_g^2}{c} Q_{pr} = \frac{L}{4\pi R^2} \frac{\pi r_g^2}{c} Q_{pr} \tag{3.56}$$

where $M_\odot$ is the mass of the Sun, L is the solar luminosity, Φ is the radiation flux density, and Q_{pr} is the solar radiation pressure coefficient. This coefficient is given by the expression $Q_{pr} = Q_{abs} + Q_{sca}(1 - \langle \cos \alpha \rangle)$, considering the particle's absorption (Q_{abs}) and scattering (Q_{sca}) coefficients. In the case of total absorption ($Q_{abs} = 1$) and perfect transmission ($Q_{pr} = 0$), we assume $Q_{pr} = Q_{abs} = 1$.

The ratio between the radiation and gravitational forces defines the parameter β (Burns et al. 1979):

$$\beta = \frac{F_{RP}}{F_G} = \left(\frac{3L}{16\pi G M c} \right) \left(\frac{Q_{pr}}{\rho r_g} \right) = 5.7 \times 10^{-5} \frac{Q_{pr}}{\rho_g r_g} \tag{3.57}$$

This parameter depends only on the properties of the particle and the Sun as the radiation source.

The resulting force on the particle is given by:

$$\vec{F} = m\dot{\vec{V}} \cong \beta \left(\frac{GM}{R^2} \right) \left[\left(1 - \frac{\dot{r}}{c} \right) \widehat{s} - \frac{\vec{V}}{c} \right] \tag{3.58}$$

where the constant component corresponds to the radiation pressure:

$$F_{RP} = \beta \left(\frac{GM}{R^2} \right) \tag{3.59}$$

and the velocity-dependent component corresponds to the Poynting-Robertson drag:

$$\vec{F}_{PR} = \left[\left(1 - \frac{\dot{r}}{c} \right) \widehat{s} - \frac{\vec{V}}{c} \right] \tag{3.60}$$

where $\dot{r}$ represents the time derivative of the position vector, and $\vec{V}$ corresponds to the velocity relative to the Sun.

The Poynting–Robertson drag decreases the orbital energy of particles on planetocentric orbits, with the energy measured relative to the planetary system rather than the Sun. In a planetocentric motion, small variations in the Sun–planet distance are neglected (so that the solar flux is constant and equal to its value relative to the planet), the planet's orbit is assumed to be circular, and planetary shadows are not considered.

Introducing into expression (3.58) the considerations corresponding to a planetocentric orbit, leads to (Mignard 1984):

$$\vec{F} = \beta \left(\frac{GM}{r_{sp}^2} \right) Q_{pr} \left[1 - \frac{\vec{r_{sp}}}{r_{sp}} \left(\frac{\vec{V_p}}{c} + \frac{\vec{V}}{c} \right) \frac{\vec{r}_{sp}}{r_{sp}} - \frac{\vec{V_p} + \vec{V}}{c} \right] \tag{3.61}$$

where $\vec{V_p}$ is the orbital velocity of the planet, $\vec{V}$ is the velocity of the particle relative to the planet and r_{sp} is the Sun–planet vector.

Radiation pressure does not modify the semi-major axis of the particles. This occurs because, in order to modify the semi-major axis, work must be performed. However, in the case of solar radiation, the force field remains constant and does not transfer energy to the particle, provided that it completes an orbit and returns to its initial position. In contrast, the eccentricity of the particles changes periodically, depending on the sin of the angle between the solar direction and the line of apsides. This periodicity is associated both with the orbital motion of the planet and with the displacement of the pericenter relative to the inertial reference frame (Burns et al. 1979). Furthermore, particles with higher inclinations exhibit more significant variations. Particle sources are predominantly located at low inclinations, and as a consequence, particles spend most of their lifetimes at low inclinations.

Small particles, with sizes of a few tens of micrometers, are strongly influenced by radiation pressure, resulting in radial dispersion both toward and away from the central body (Verbiscer et al. 2009).

The analytical calculation of the decay time τ_{PR} can be performed using the following expression (Burns et al. 1979):

$$\tau_{PR} = 9.3 \times 10^6 \frac{R^2 \rho r}{Q_{pr}} \quad \text{(years)} \tag{3.62}$$

where R is the heliocentric distance of the planet.

We analyzed the decay time of particles due to Poynting-Robertson drag for particles of different sizes (see in Figure3.2). We considered particles with a density of 1 g/cm^3 and radii ranging from 1 to 100 μm. It can be observed that smaller particles exhibit significantly shorter decay times, on the order of 10^5 years, and are quickly removed from the system. As the particle radius increases, the decay time also increases, reaching values close to 10^7 years for 100 μm particles. This behavior reflects the direct dependence of τ_{PR} on particle size, indicating that larger particles are much more stable under the effect of Poynting-Robertson drag, remaining in orbit for substantially longer periods of time.

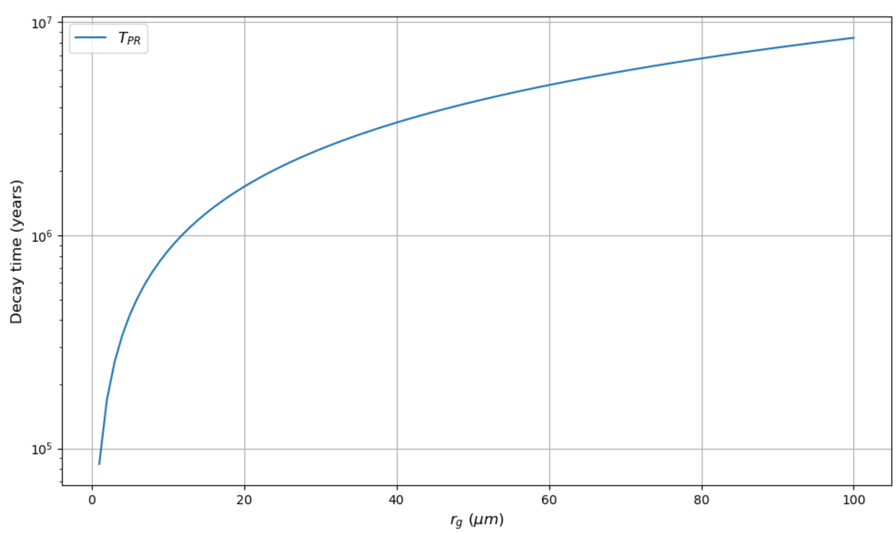

Figure 3.2: Decay time of particles with radii ranging from 1 μm to 100 μm.

From Eq. 3.58, we can obtain the expression for the disturbing potential (V_{RP}). Since the magnitude and direction of the radiation pressure vary slightly over a single orbit of the dust grain, we can consider the right-hand side of Eq. 3.58 as a constant. Therefore, we obtain $V_{RP} = F_{RP}(s_x\widehat{x} + s_y\widehat{y} + s_z\widehat{z})$. By expressing the Cartesian coordinates x, y, z in terms of the orbital elements and substituting the potential into the planetary equations (Danby 1988), we derive the equations that describe the effect of the solar radiation force on the dust particle orbits.

$$\left\langle \frac{da}{dt} \right\rangle_{RP} = 0, \tag{3.63}$$

$$\left\langle \frac{de}{dt} \right\rangle_{RP} = \alpha(1-e^2)^{1/2}\big[s_x(\cos\Omega\sin\omega + \sin\Omega\cos\omega\cos I)+$$
$$+ s_y(\sin\Omega\sin\omega - \cos\Omega\cos\omega\cos I) - s_z(\cos\omega\sin I)\big], \tag{3.64}$$

$$\left\langle \frac{dI}{dt} \right\rangle_{RP} = \frac{\alpha e}{(1-e^2)^{1/2}}\big[s_x(\sin\Omega\cos\omega\sin I) + s_y(\cos\Omega\cos\omega\cos I)+$$
$$- s_z(\sin\omega\cot I)\big], \tag{3.65}$$

$$\left\langle \frac{d\Omega}{dt} \right\rangle_{RP} = \frac{\alpha e}{(1-e^2)^{1/2}\sin I}\big[s_x(\sin\Omega\sin\omega) - s_y(\cos\Omega\sin\omega) - s_z(\cos\omega\cot I)\big], \tag{3.66}$$

$$\left\langle \frac{d\omega}{dt} \right\rangle_{RP} = \frac{\alpha(1-e^2)^{1/2}}{e}\big[s_x(\cos\Omega\cos\omega - \sin\Omega\sin\omega\cos I) + s_y(\sin\Omega\cos\omega+$$
$$+ \cos\Omega\cos\omega\cos I) + s_z(\sin\omega\sin I)\big] - \cos I\left\langle \frac{d\Omega}{dt} \right\rangle_{RP}, \tag{3.67}$$

$$\left\langle \frac{dM}{dt} - n \right\rangle_{RP} = -\frac{\alpha(1+e^2)}{e}\big[s_x(\cos\Omega\cos\omega - \sin\Omega\sin\omega\cos I) + s_y(\sin\Omega\cos\omega+$$
$$+ \cos\Omega\cos\omega\cos I) + s_z(\sin\omega\sin I)\big]. \tag{3.68}$$

From Equation 3.68, we see that the semi-major axis does not change due to the solar radiation force. This occurs because the force generated by the potential is conservative and, therefore, does not affect the size of the orbit.

The trigonometric terms oscillate periodically as ω and Ω vary over time, leading to periodic variations in eccentricity. Therefore, forces affecting the orbit's pericenter, such as those associated with planetary oblateness and electromagnetic interactions, can cause an increase or decrease in eccentricity.

Similarly to eccentricity, the inclination also varies periodically. The variations in inclination depend on the eccentricity and the direction of the disturbing force (s_x, s_y, s_z).

3.1.5 Plasma drag

In this section, we analyze the influence of the plasma drag force on particles present in a plasma environment. First, we explore the different types of drag associated with the plasma environment, describing their main characteristics. Then, we explore in detail the regimes involved and the equations that describe these forces in each case.

In the context of the forces mentioned, plasma drag arises as an important factor affecting the trajectories of charged particles. This phenomenon occurs due to the interaction between dust particles and the plasma present in the environment, resulting in collisions that generate two types of forces: ion drag and Coulomb drag. Each of these forces is dominant in distinct regimes.

When considering only direct collisions between the plasma and the dust grain, the acting force is the ion drag (*ionic drag*). Morfill et al. (1980), described by the following equation:

$$F_d = -N_h \pi s^2 m_i u^2 \left[\frac{v}{u} \frac{1}{\sqrt{\pi}} e^{-\left(\frac{v}{u}\right)^2} + \left(\frac{v}{u} + \frac{1}{2} \right) erf\left(\frac{v}{u} \right) \right] \tag{3.69}$$

where N_h is the plasma density, s is the dust grain radius, m_i is the average ion mass, u is the ion velocity, v is the dust particle velocity, and erf is the error function.

On the other hand, when long-range (Coulomb) collisions are considered, the particle experiences momentum loss due to Coulomb drag (*Coulomb drag*) Morfill et al. (1980), given by the following equation:

$$F_c = 2\sqrt{\pi} n_i m_i \alpha^2 \frac{1}{u} \int_{-\infty}^{\infty} dw \frac{(w-v)}{|w-v|^3} e^{-\frac{w^2}{u^2}} log \frac{1 + \left(\frac{\lambda_d}{\alpha}\right)^2 (w-v)^4}{1 + \left(\frac{s}{\alpha}\right)^2 (w-v)^4} \tag{3.70}$$

where n_i is the density of the ion, $\alpha = Qe/m_i$, with Q being the charge of the dust grain and e the ion charge, and λ_d represents the Debye length, given by:

$$\lambda_d = \left(\frac{kT_e}{4\pi n_i e^2} \right)^{\frac{1}{2}} \tag{3.71}$$

where k is the Boltzmann constant and T_e is the ion temperature.

Equations 3.69 and 3.70 can be simplified depending on the regime considered, based on the grain velocity relative to the plasma:

- **Supersonic Regime:** When $v > u$, that is, $\frac{v}{u} \gg 1$, the influence of direct collisions is more significant, and equation 3.69 reduces to:

$$F_d = -\pi n_i s^2 m_i v^2 \tag{3.72}$$

- **Subsonic Regime:** When $v < u$, that is, $\frac{v}{u} \ll 1$, Coulomb collisions are more significant, and Equations (3.69) and (3.70) reduces to:

$$F_d = -2\sqrt{\pi} n_i s^2 m_i u v \tag{3.73}$$

$$F_c = -2\sqrt{\pi} n_i m_i v u s^2 \int_{\infty}^{0} dx \frac{1}{x} e^{-x^2} log \frac{1 + \left(\frac{2\lambda_d}{s}\right)^2 x^4}{1 + 4x^4} \tag{3.74}$$

With an understanding of the disturbing forces involved in this study, we proceed to investigate which of them predominates in different orbital regions, considering the distance to the planet.

3.2 Magnitude of the forces

Dust particles present in planetary systems are subject to a complex set of gravitational and non-gravitational forces, the relative importance of which depends on their orbital location, size, and physical properties. In certain dynamical regimes, a single perturbation may dominate over the others, allowing the orbital evolution to be satisfactorily described by simplified models. However, in other regions of the system, particularly those simultaneously influenced by the planet, its satellites, the magnetic field, solar radiation, and plasma drag, multiple effects act with comparable intensities. In such cases, the resulting dynamics becomes intrinsically more complex, requiring an approach that incorporates the combined action of these perturbations in order to achieve a realistic description of the orbital evolution.

In this section, we analyze the intensity of the different forces as a function of the distance from the planet, with the exception of those associated with plasma drag. In this way, it becomes possible to identify which perturbation dominates the particle dynamics in each region of the system.

To simplify the analysis, we consider the planar case, assuming that the orbital motion is confined to two spatial dimensions. In addition, we assume that the planets move on circular orbits around the Sun and that the perturbations on the orbit of a dust grain are averaged over one planetary orbit.

For each perturbing force, Hamilton & Krivov (1996) introduced dimensionless parameters in order to describe the strength of these perturbations as a function of the distance from the planet. These parameters are dimensionless because they represent the magnitude of each perturbing force relative to the planet's gravitational force. They depend on the particle's semi-major axis, as well as on the physical properties of both the planet and the dust grain.

For the parameter associated with planetary oblateness (W), described in Equation 3.75, we consider only the J_2 term, as it provides the leading contribution relative to the higher-order even harmonics.

$$W = \frac{3}{2} J_2 \left(\frac{R}{a} \right)^2 \frac{n}{n_\odot} \tag{3.75}$$

where J_2 is the second-order zonal harmonic coefficient, R is the planetary radius, a is the particle's semi-major axis, $n_\odot$ is the mean motion of the planet around the Sun, and n is the mean motion of the particle.

The parameter associated with the Lorentz force is given by:

$$\tilde{L} = 2 \frac{n}{n \odot} \frac{n}{\Omega_p} L \tag{3.76}$$

where Ω_p is the planet's angular rotation rate and L is the parameter defined by:

$$L = \frac{q g_{1,0} R_p^3 \Omega_p}{G M_p m_g c} \tag{3.77}$$

where $g_{1,0}$ is the Gauss coefficient, R_P is the planetary radius, G is the gravitational constant, M_p is the planetary mass, m_g is the mass of the dust grain and c is the speed of light.

The radiative parameter C is defined by the expression:

$$C = \frac{3}{4} \frac{n_\odot}{n} \sigma \tag{3.78}$$

where σ is the ratio between the radiation pressure force and the gravitational force.

$$\sigma = \frac{F_{RP}}{F_G} = \frac{3}{4} Q_{pr} \frac{\Phi a^2}{G M_p c \rho_g r_g} \tag{3.79}$$

where Q_{pr} is the radiation pressure efficiency coefficient, Φ is the solar flux at the planet's heliocentric distance, and ρ_g and r_g are the particle's density and radius, respectively.

We calculated all these parameters for particles of 1 μm and 10 μm around Saturn, as shown in Figure 3.3.

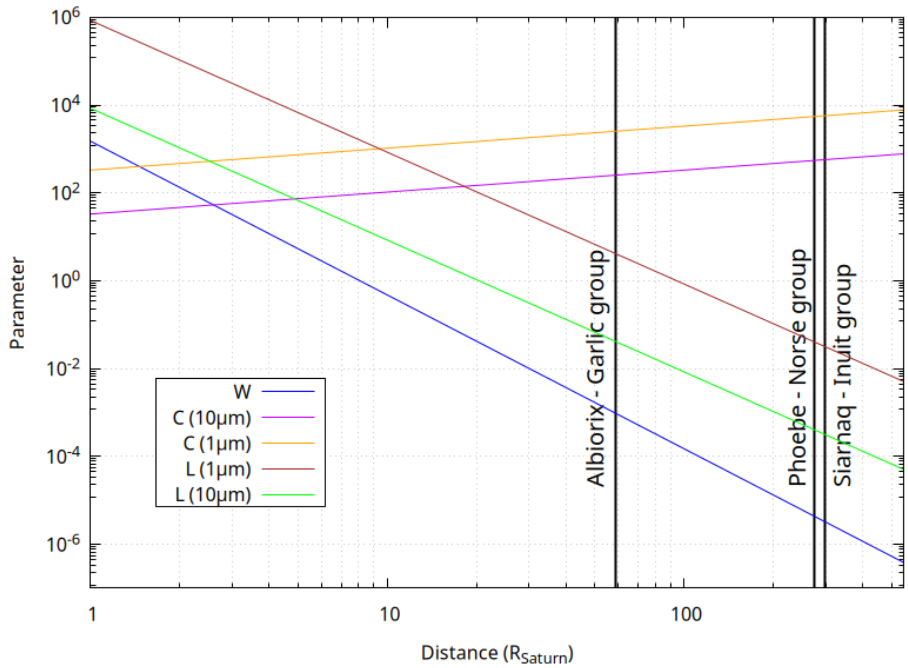

Figure 3.3: Dimensionless parameters of the perturbative forces as a function of the distance from the planet. W represents oblateness, C solar radiation, and L the Lorentz force. The vertical line indicates the location of Saturn's families. We assume a particle density of $\rho_g = 1gcm^{-3}$, a charge of $\Omega_g = 5V$, and particle sizes of 1 μm and 10 μm.

In the region between $1R_s$ and $2R_s$, the dynamics of the particles are dominated by oblateness and electromagnetic forces. In the range from $2R_s$ to $13R_s$, there is a competition between the oblateness and electromagnetic forces and the solar radiation force. Beyond $13R_s$, the effect of solar radiation becomes predominant. In general, the oblateness and electromagnetic forces decrease with distance from the planet, while the solar radiation force increases as the dust particles move farther away.

Furthermore, we see that the effect of the solar radiation force is significantly stronger (by two orders of magnitude) for 1 μm particles compared to 10 μm particles. This behavior is expected, since the parameter C is inversely proportional to the grain radius, as described in Equation 3.78.

3.3 Dust production

One of the mechanisms responsible for generating dust present in rings, around satellites, and even migrating throughout the Solar System is the collision of interplanetary projectiles (IDPs) with the surfaces of satellites. Micrometeoroids impacting satellites originate from two main sources: interplanetary dust captured by the planet's gravity and dust native to the planetary system. Dust orbiting the planet has a lower relative velocity, transferring less kinetic energy to the satellites. This type of dust becomes relevant only at very high densities, such as in Saturn's E ring (Porter et al. 2010). Measurements from the Cassini spacecraft indicate that Enceladus is the primary source of the E-ring dust (Spahn et al. 2006). However, the main source of micrometeoroids impacting satellite surfaces remains interplanetary dust. The principal sources of IDPs are cometary families (Dikarev et al. (2005); Nesvorný et al. (2010); Poppe & Horányi (2011)) and the Kuiper Belt (EKB) (Landgraf et al. 2002). In this section, we compute the IDP flux at Saturn's orbit and the amount of material produced by its satellites.

Measuring the density of IDPs through observational methods presents significant challenges. For this reason, the use of spacecraft to perform in situ analyses has demonstrated to be the most effective approach. Previous studies have investigated the distribution of solid particles at various heliocentric distances. Grün et al. (1985) analyzed data obtained primarily from spacecraft near Earth and determined the flux of IDPs with masses up to $1g$ at $1AU$. These results were later adapted for other masses and heliocentric distances, as presented by Colwell & Esposito (1990).

According to Porter et al. (2010), the mass flux of IDPs in the vicinity of Saturn is approximately $1.8 \times 10^{-16} kg m^{-2} s^{-1}$. We assume that the velocity of IDPs near Saturn is given by the average speed of grains originating from the EKB, $v_{imp}^{(\infty)} = 3.1 km/s$ (Poppe 2016), and that the mass of the impactors is $m_{imp} = 10{-}8 kg$.

When an interplanetary projectile crosses into Saturn's Hill sphere, both its velocity and flux increase. The mechanism responsible for this effect is gravitational focusing (Colombo et al. 1966).

$$\frac{v_{imp}}{v_{imp}^{\infty}} = \sqrt{1 + \frac{2GM_{\odot}}{r(v_{imp}^{\infty})^2}} \tag{3.80}$$

This expression relates the velocity of the particle before gravitational focusing (v_{imp}) to its velocity after the effect (v_{imp}^{∞}).

As the particles approach the planet, the number density of projectiles (n_{imp}^{∞}) is modified to (n_{imp}).

$$\frac{n_{imp}}{n_{imp}^{\infty}} = \frac{1}{2}\frac{v_{imp}}{v_{imp}^{\infty}} + \frac{1}{2}\left[\left(\frac{v_{imp}}{v_{imp}^{\infty}}\right)^2 - \left(\frac{R_S}{r}\right)^2\left(1 + \frac{2GM_\odot}{R_S(v_{imp}^{\infty})^2}\right)\right]^{\frac{1}{2}} \tag{3.81}$$

The mass flux of IDPs at an orbital radius r is computed from the expression that relates the velocity and number density of the projectiles before and after gravitational focusing (Colombo et al. 1966, Krivov et al. 2003):

$$\frac{F_{imp}}{F_{imp}^{\infty}} = \frac{1}{2}\left(\frac{v_{imp}}{v_{imp}^{\infty}}\right)^2 + \frac{1}{2}\frac{v_{imp}}{v_{imp}^{\infty}}\left[\left(\frac{v_{imp}}{v_{imp}^{\infty}}\right)^2 - \left(\frac{R_S}{r}\right)^2\left(1 + \frac{2GM_\odot}{R_S(v_{imp}^{\infty})^2}\right)\right]^{\frac{1}{2}} \tag{3.82}$$

3.4 Dust production rate

In our Solar System, the production of dust particles from collisions with IDPs is the most important mechanism responsible for maintaining several structures, such as Saturn's E ring (Horanyi et al. 1992) and Jupiter's rings (Morfill et al. 1980).

Based on the work of Sfair & Giuliatti Winter (2012), we calculated the dust production rate (M^+) using the direct impact model, in which the projectile collides with the satellite's surface:

$$M^+ = F_{imp} Y S \tag{3.83}$$

where F_{imp} is the flux of impactors on the satellite's surface, Y is the ejecta yield, and S is the cross-sectional area.

In our case, we considered a satellite composed of pure ice (without silicates, that is, $G_{SIL} = 0$). Therefore, the yield can be expressed as (Madeira et al. 2018):

$$Y = 2.64 \times 10^{-5} m_{imp}^{0.23} v_{imp}^{2.46} \tag{3.84}$$

For an impactor with a radius of approximately 100 μm, the mass is $m_{imp} = 10^{-8} kg$, and the impact velocity is $v_{imp} = 5.886 \times 10^4 ms^{-1}$, resulting in a yield of $Y = 3.511 \times 10^5$.

From these collisions, the dust production rate for projectiles impacting Iapetus is:

$$M^{+} = 1.039 \times 10^{7}\,\mathrm{kg\ s^{-1}} \tag{3.85}$$

We analyzed satellites with radii of approximately 30 km or smaller, since for satellites with sizes larger than this the escape velocity increases to the point where dust ejection is significantly reduced.

We calculated M^{+} for all Saturnian satellites (Tables A.1 to A.5) and identified that the dust production rate is directly proportional to the satellite's radius. We examined the satellites belonging to each dynamical group, Gallic, Inuit, and Norse, noting that these groups were defined according to their inclinations and eccentricities.

For the Gallic group, we analyzed Albiorix (radius 13km) and Bebhionn (radius 3km), and the corresponding production rates were 1.411×10^{-4} kg s^{-1} and 7.397×10^{-6} kg s^{-1}, respectively. Considering the other cases, we found that the satellite producing the largest amount of dust in the Inuit group is Siarnaq, with a rate of 2.041×10^{-4} kg s^{-1}, while in the Norse group the most productive satellite is Ymir, with 5.656×10^{-5} kg s^{-1}.

We computed the parameters described in Eqs. 3.80–3.85 for the innermost and outermost natural satellites of the Saturnian system, defined here as the satellites located at the minimum and maximum orbital distances from Saturn. The calculations assume a representative impactor with mass $m_{imp} = 10^{-8}$ kg, corresponding to a particle with a characteristic size of approximately 100 μm. The resulting dust production parameters are summarized in 3.1.

Table 3.1: Dust Production Parameters in the Saturnian System Calculated for the Innermost and Outermost Satellites.

	Innermost satellite	**Outermost satellite**
v_{imp}/v_{imp}^{∞}	206.01	18.92
n_{imp}/n_{imp}^{∞}	311.14	190.57
F_{imp}	1.15×10^{-11}	6.49×10^{-13}
M^{+}	5.03×10^{-01}	1.15×10^{-05}

From Table 3.1, it is evident that the density of projectiles (v_{imp}/v_{imp}^{∞}) increases significantly as we approach the planet. This is illustrated by the density ratio, which reaches 311.14 for the innermost satellite and decreases to 190.57 for the outermost one. In addition, particles located closer to the planet exhibit higher velocities, as expected due to the effect of gravitational focusing.

Another important point is that the dust production rate (M^{+}) on the satellites closest to the planet is about four orders of magnitude higher than that of the more distant satellites. This behavior is also consistent with theoretical studies, since the stronger gravitational influence in regions near the planet increases both the velocity and density of projectiles, resulting in a significantly greater production of dust particles.

Chapter 4

Methods

In our work, we developed a model to explain the origin and subsequent evolution of dust particles in the Saturnian satellite system. With this model, we are able to analyze the particle's behavior from the moment it is ejected until the end of its lifetime, under the influence of different forces.

The preliminary analyses were organized into three stages. The first stage corresponds to the study of forces, in which we investigated separately the effects of different perturbing forces on the orbits of particles after their ejection from the satellites. In this stage, the system was simulated for 500 years. Separate simulations were performed for particles with radii of 1 μm and 100 μm ejected from Rhea and Siarnaq, in order to compare the behavior of particles located closer to the rings with those situated in regions farther from the planet. For each case, a single simulation was performed considering one particle, with Rhea and Siarnaq analyzed in separate simulations.

The second stage corresponds to the study of the families, in order to analyze the behavior of particles ejected from different regions of these families. We randomly inserted 5 particles in the regions associated with each family, considering the ranges of orbital elements presented in Table 2.1, with one simulation performed for each family. In this stage, we studied particles with radii of 1 and 10 micrometers, simulating the system for 3500 years with the inclusion of all perturbing forces.

Finally, the third stage corresponds to the study of the satellites, in which we analyzed the behavior of particles when ejected from these bodies and tracked their orbital evolution over time. In this step, we included 76 satellites in the simulations. For particle ejection, we selected the largest satellite of each family: Albiorix, in the Gallic family; Ymir, in the Norse family; and Siarnaq, in the Inuit family. We simulated 100 particles with radii of 10 μm over 5000 years, considering all perturbing forces. Only particles of 10 μm were considered because previous analyses indicated that particles of 1 μm would not survive in this region, while particles of 100 μm would be only weakly affected by the perturbing forces. In this stage, collisions with the planet and with the satellites were detected when the distance between the particle and the body became smaller than the body's radius.

Based on all the information obtained from our system through the preliminary analyses, we developed a C code to simulate the Saturnian system, considering 15 satellites and 50 dust particles. Only satellites with radii smaller than 30 km were included, since larger bodies have a low probability of generating dust due to their high escape velocity. In this final stage, Albiorix, Phoebe, and Siarnaq were selected as representatives of the Gallic, Norse, and Inuit families, respectively, being the largest satellites of each group within the considered limit. The objective was to investigate if the particles remained within the region associated with their original family or were transported to other areas of the system.

Due to the micrometric size of the particles, the solar radiation force was considered, as it induces a significant influence on small bodies. In addition, we included the effect of planetary oblateness, since Saturn is the most oblate planet in the Solar System, which impacts orbital dynamics around its equator. The electromagnetic force was also included, given Saturn's intense magnetic field, which interacts directly with charged particles. Finally, we considered plasma drag, which affects particle orbits in regions up to 20 Saturn radii (R_s), contributing to the evolution of their trajectories. Collisions between dust particles and Saturn were recorded, and once a collision is detected, the particle is removed from the system. Furthermore, we consider that a particle is ejected from the Saturnian system when its orbit becomes hyperbolic, that is, when its eccentricity reaches 1.

In our case, the transport of particles throughout the Saturnian system implies that, at some stage of their evolution, each force becomes relevant, as illustrated by the intensity diagram; consequently, none of them can be neglected in the simulations. As shown in the plot in Figure 3.3, the closer a particle is to the planet, the greater the influence of the Lorentz force and planetary oblateness, while the farther it is, the stronger the solar radiation pressure force along its orbit.

As shown in the plot in Figure 3.3, the intensity of the solar radiation force reaches the order of 10^4. This supports the hypothesis that the solar radiation force acting on 1 micrometer particles in the regions of the Inuit, Norse, and Gallic groups is strong enough to eject them from the system almost instantaneously. The forces of planetary oblateness, electromagnetic force, and solar radiation were implemented based on the work of Siqueira (2019), while the plasma drag force was validated according to Morfill et al. (1980). The spherical harmonic coefficient $J_2 = 16298 \times 10^{-6}$ was obtained from Campbell & Anderson (1989), while the magnetic field coefficient $g_{1,0} = 0.2154$ was taken from Schaffer & Burns (1992).

All particles ejected from the satellites were released at a distance of 1.01 times the satellite radius to prevent initial collisions. They were distributed isotropically throughout the region, with an ejection velocity equal to 1.5 times the satellite escape velocity, described by the following expression:

$$V_{esc} = \sqrt{\frac{2GM_{sat}}{R}} \tag{4.1}$$

where M_{sat} and R are the mass and radius of the satellite from which the particles will be ejected, respectively.

The particles were ejected from different satellites of the Saturnian families, with the objective of analyzing the differences in the behavior of dust particles when launched in regions with distinct initial conditions. Additionally, we analyzed the amount of time these particles remain within their each family after ejection.

We tracked the behavior of the particle from the moment it is ejected from the satellite until it reaches one of the sinks: collision with Saturn, collision with the satellites, or ejection from the system.

The particles were considered as test particles, meaning that they do not gravitationally interact with one another. However, they are affected by the gravitational forces of the planet and the satellites, as well as by the other perturbing forces included in the model.

With respect to dust ejected from the satellites, we performed the analytical calculation of the dust production rate for all satellites. In this step of the work, we considered only satellites with radii smaller than 30 km, since the probability of dust ejection from larger bodies is small due to their high escape velocity. The code used to calculate the dust production rate was validated based on the work of Sfair & Giuliatti Winter (2012).

The numerical integrations were performed using the IAS15 integrator from the REBOUND package (Rein & Spiegel 2015). The REBOUND package is used to study the motion of N bodies under gravitational forces, but it also allows, through external libraries, the inclusion of other non-gravitational forces. We selected the IAS15 integrator due to its high accuracy and non-symplectic nature, allowing the use of adaptive time steps. It can analyze close encounters, high eccentricities, conservative and non-conservative forces, while keeping systematic errors below machine precision.

With the developed code, we have a solid basis for studying the transport of dust particles in other systems, such as Jupiter's system, for example. We can modify the initial conditions and evaluate the need to include other relevant perturbations in the system of interest.

Chapter 5

Results

In this section, we analyze the results obtained in our study, exploring the trajectories of the particles for different initial conditions. We analyze the behavior of the particles with each perturbative force considered separately, the dynamics associated with the introduction of particles into the different satellite groups, the behavior of the particles ejected from the satellites, and, finally, the resulting trajectories when all these analyses are considered in combination.

5.1 The effect of forces on particles

Analyzing the effect of each perturbative force on the particles individually facilitates the identification of the specific contribution and influence of each force when interpreting the results obtained with all forces acting simultaneously.

In this stage of the work, we considered a system involving Saturn, a single particle with radii of 1 μm and 100 μm, a density of 1 gcm^{-3}, and the perturbative forces included individually. The particles were inserted into two different source regions: the orbits of Rhea (8.8 R_s) and Siarnaq (278 R_s), and the system was simulated for 500 years.

For the case of the planetary oblateness force acting on a particle with a radius of 1 μm, we obtained the results ilustrated in Figure 5.1. The behavior of the orbital elements is consistent with the averaged equations for their variation described in section 3.1. The semi-major axis, eccentricity, and inclination are not affected by this force, while the longitude of the ascending node and the argument of pericenter present periodic variations. The effect of oblateness on particles with radii of 100 μm was similar to that observed for particles with radii of 1 μm, since this force is independent of particle size.

For the electromagnetic force, we considered particles with a charge of –5 V, and the results are shown in Figure 5.2.

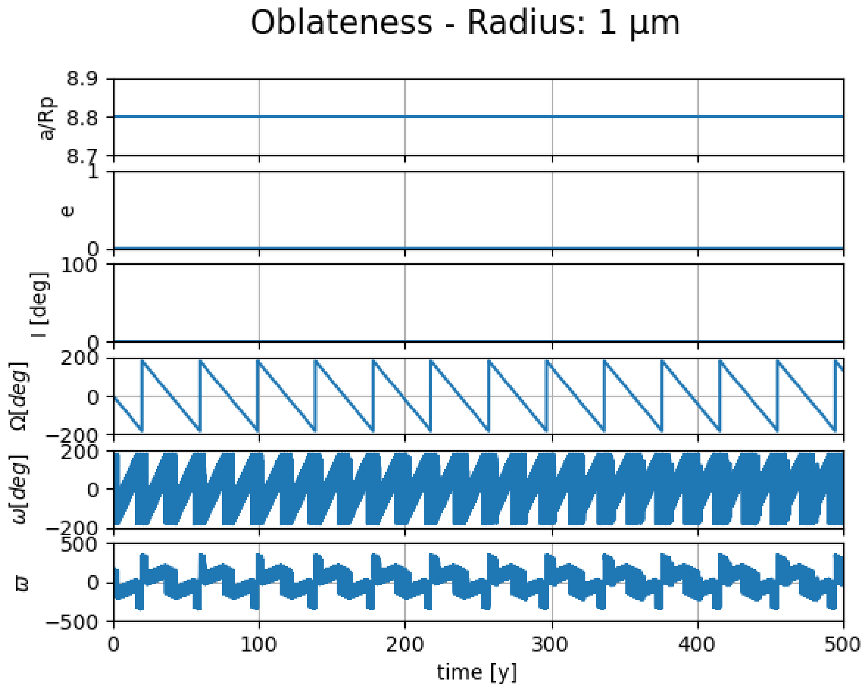

Figure 5.1: Impact of the planetary oblateness force, considering the J_2 term, on the orbits of 1 μm particle, initially inserted at Rhea's orbit (8.8 R_s), over a period of 500 years.

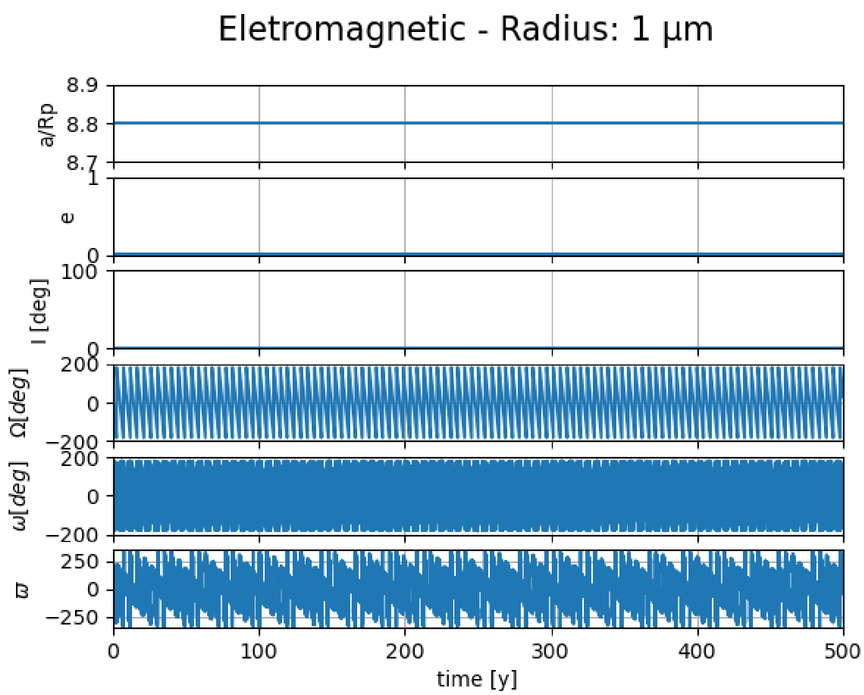

Figure 5.2: Impact of the electromagnetic force on the orbits of 1 μm particle, initially inserted at Rhea's orbit (8.8 R_s), over a period of 500 years.

From Figure 5.2, we observe a similar behavior to the case of planetary oblateness: the semi-major axis, eccentricity, and inclination remain unchanged, while the longitude of the ascending node and the argument of pericenter vary periodically. The effect of the electromagnetic force does not change significantly with particle size, as particles with a radius of 100 μm exhibit the same dynamical behavior as those with smaller radii within the adopted model.

The result obtained for the radiation force, including both the Poynting–Robertson and radiation pressure components and considering micrometer-sized particles, are shown in Figure 5.3.

Analyzing Figure 5.3, we observe that the semi-major axis decreases over time due to the Poynting–Robertson drag, while the eccentricity varies periodically due to radiation pressure. In contrast to the previously analyzed forces, there is a significant difference in the behavior of particles of different radii: the 1 μm particle is much more affected by solar radiation than the 100 μm particle.

The semi-major axis of the 1 μm particle decreases over time, while that of the 100 μm particle does not present a significant variation. With respect to the eccentricity, it oscillates periodically between 0 and 1 for the 1 μm particle, while for the 100 μm particle the variation is much smaller, ranging between 0 and 0.02. The remaining orbital elements also exhibit periodic variations with different patterns, but the amplitude of the motion is similar for particles of both radii.

Comparing the two plots associated with solar radiation, we conclude that smaller particles are more significantly influenced by solar radiation than larger particles. This behavior was expected, since the solar radiation force is inversely proportional to particle radius and therefore affects smaller particles more strongly.

For the plasma drag force, we obtained the result illustrated in Figure 5.4. We see that the plasma force causes the particles to migrate farther from the planet. In addition, as the particle radius increases, the effect of this force decreases.

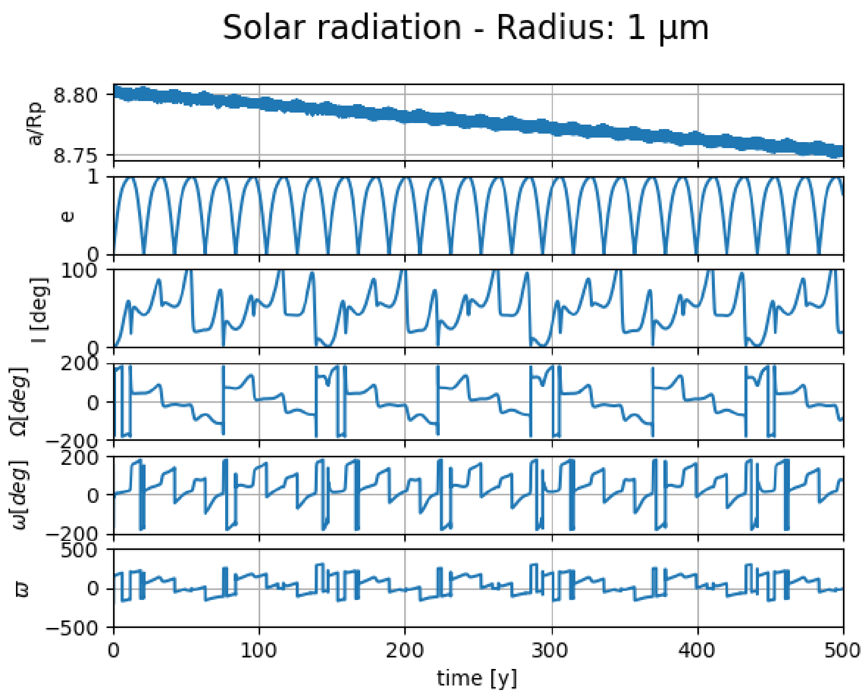

(a)

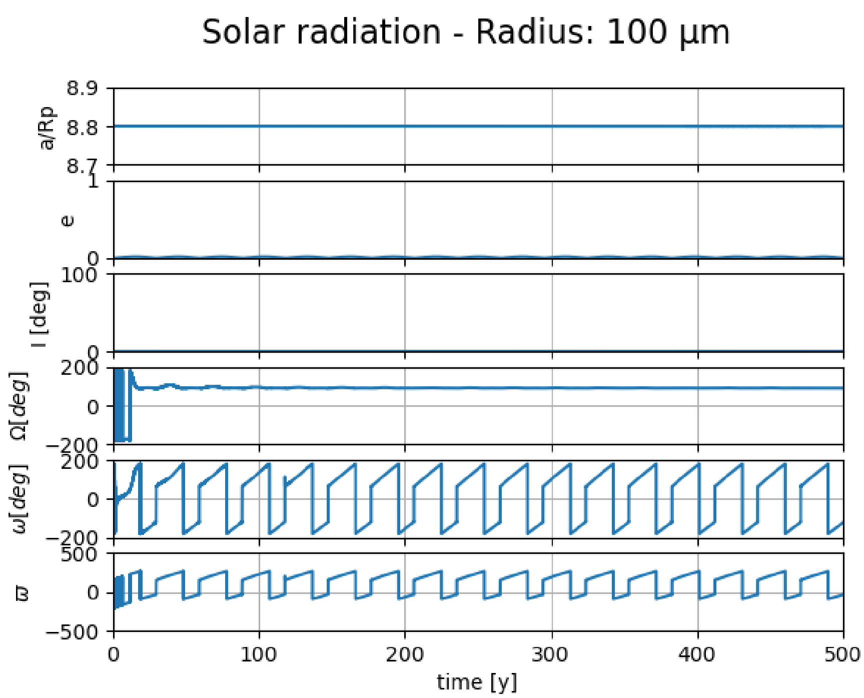

(b)

Figure 5.3: Impact of the solar radiation force on the orbits of (a) 1 μm and (b) 100 μm particles, initially inserted at Rhea's orbit (8.8 R_s), over a period of 500 years.

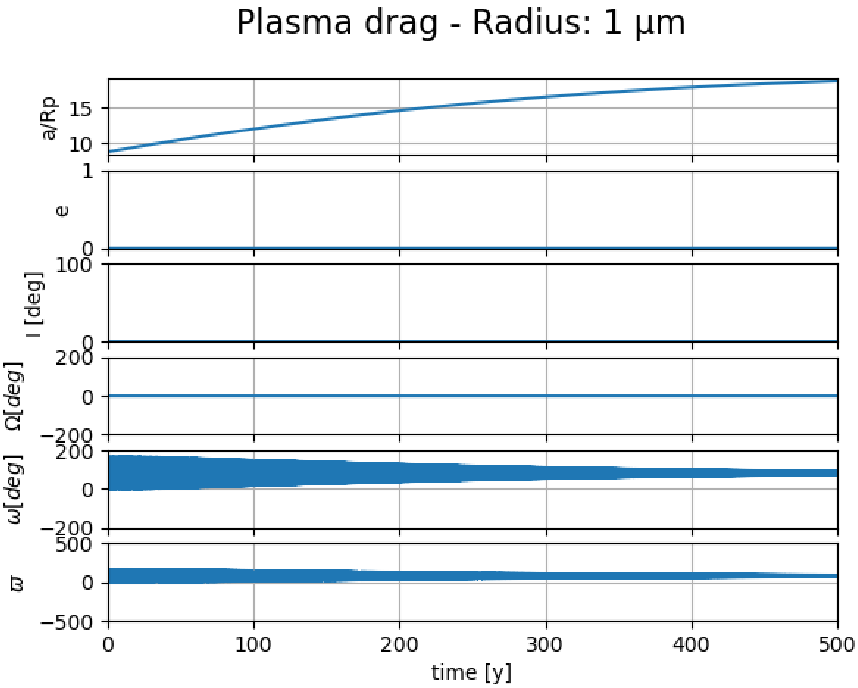

(a)

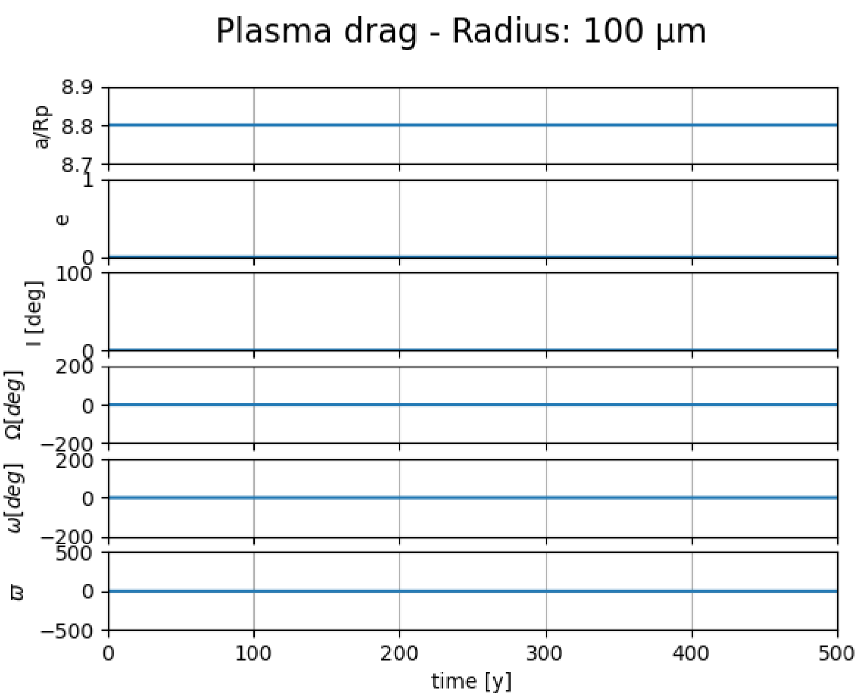

(b)

Figure 5.4: Impact of the plasma drag force on the orbits of (a) 1 μm and (b) 100 μm particles, initially inserted at Rhea's orbit (8.8 R_s), over a period of 500 years.

We also analyzed the same forces separately, but this time for particles inserted at a significantly greater distance, in Siarnaq's orbit (278 R_s), in order to investigate how the effect of these forces changes with the particles' orbital distance.

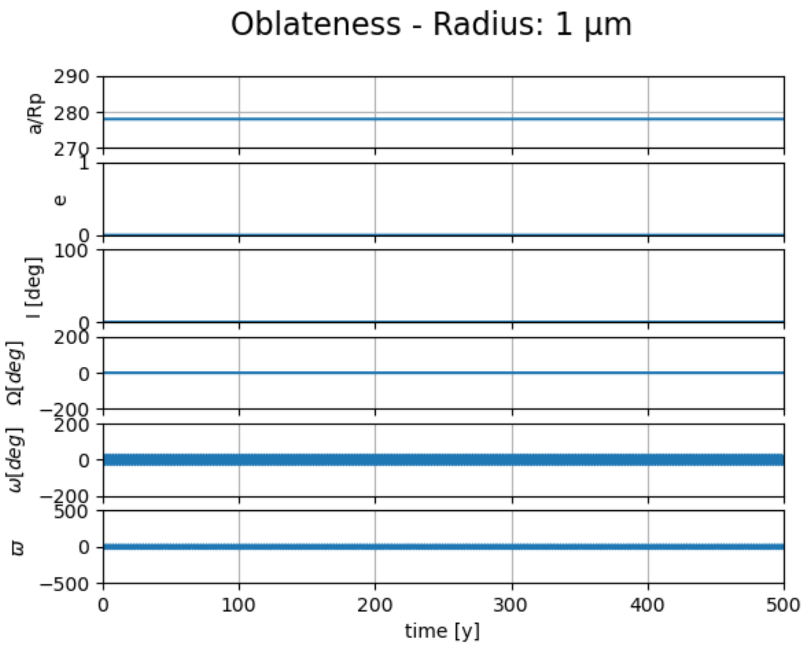

Figure 5.5: Impact of the planetary oblateness force, considering the J_2 term, on the orbits of (a) 1 μm and (b) 100 μm particles, initially inserted at Siarnaq's orbit (278 R_s), over a period of 500 years.

In the analysis of planetary oblateness (Figure 5.5), we verified that there is no significant variation in the orbital elements of the particles. A similar behavior is observed for the electromagnetic force (Figure 5.6). This occurs because, as the particle is situated farther from the planet, the effects of oblateness and the electromagnetic force decrease.

By analyzing Figure 5.1 and Figure 5.5, we see that particles inserted farther from the planet experience a smaller influence from planetary oblateness. This behavior is also observed for the electromagnetic force, as shown in the comparison between Figure 5.2 and Figure 5.6.

In the case of solar radiation, illustrated in Figure 5.7, it is observed that the particle inserted into Siarnaq's orbit is more strongly affected by the solar radiation force compared to particles located closer to the planet. This behavior occurs because the intensity of the solar radiation force increases with distance from the planet, as shown in Figure 3.3. Additionally, as the distance increases, the planet's gravitational force decreases, allowing the solar radiation force to dominate in competition with the gravitational force.

For particles with a radius of 1 μm inserted into Siarnaq's orbit, the effect of solar radiation

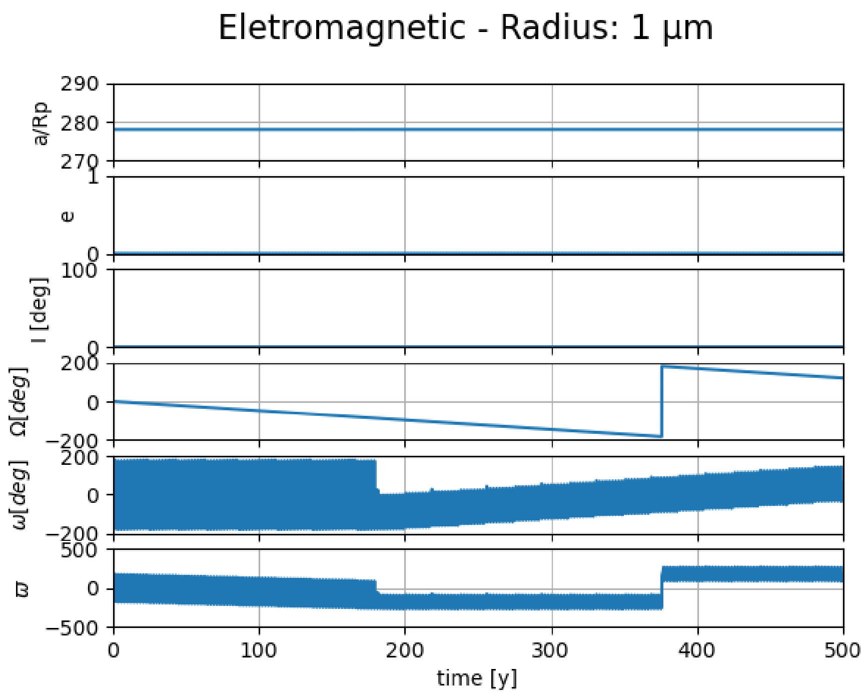

Figure 5.6: Impact of the electromagnetic force on the orbits of (a) 1 μm and (b) 100 μm particles, initially inserted at Siarnaq's orbit (278 R_s), over a period of 500 years.

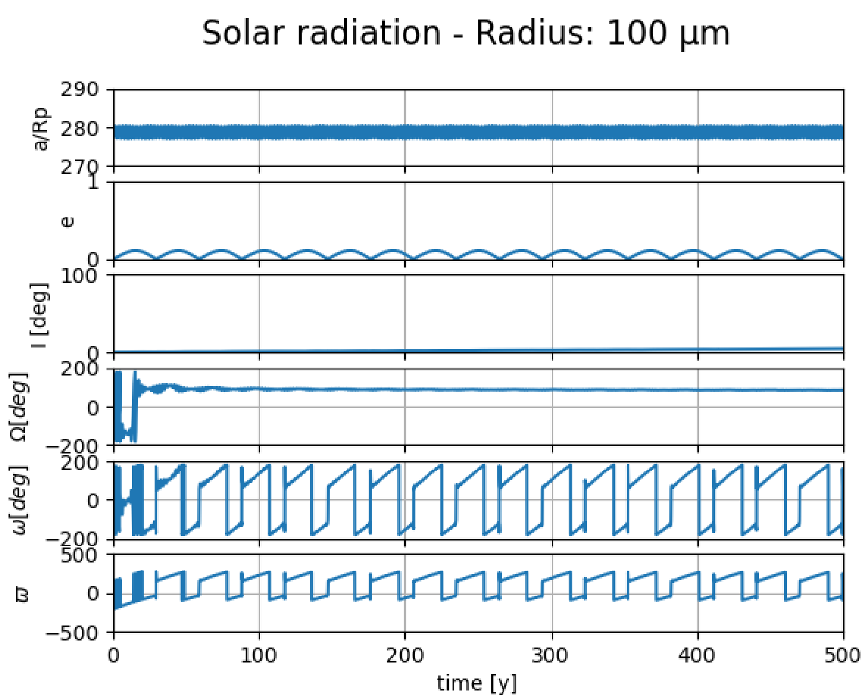

Figure 5.7: Impact of the solar radiation force on the orbits of 100 μm particles, initially inserted at Siarnaq's orbit (278 R_s), over a period of 500 years.

is so strong that the particle is ejected from the system in less than one year. For this reason, the corresponding orbital evolution is not shown in the Figure 5.7.

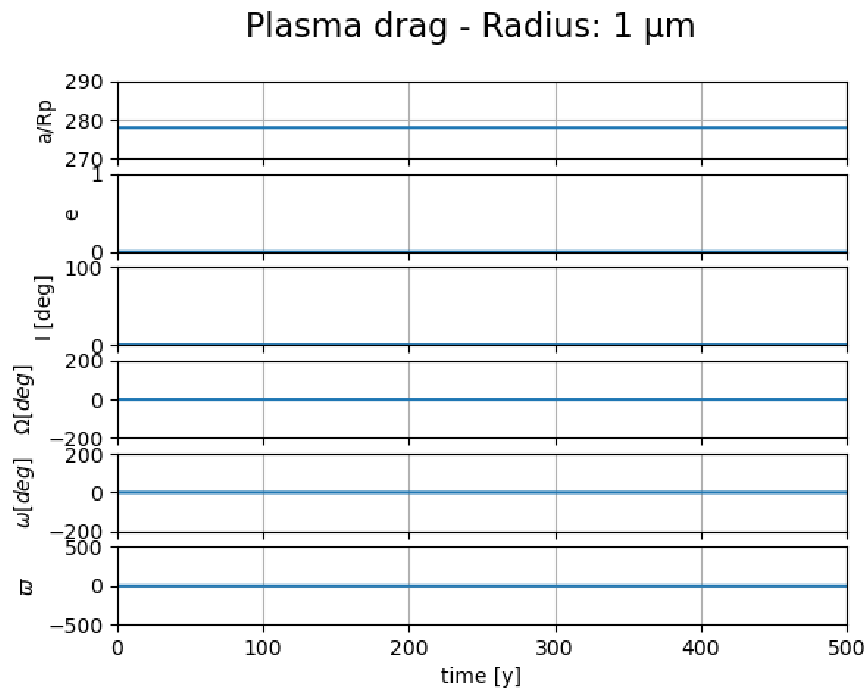

Figure 5.8: Impact of the plasma drag force on the orbits of (a) 1 μm and (b) 100 μm particles, initially inserted at Siarnaq's orbit (278 R_s), over a period of 500 years.

As shown in Figure 5.8, the orbital elements of particles with radii of 1 and 100 μm inserted in the orbit of Siarnaq remain constant throughout the integration time. This indicates that, at this distance, the plasma drag force does not exert a significant influence on the particles' orbits.

We completed the force-analysis stage by simulating a system involving Saturn, a single particle, and all forces included simultaneously.

When all forces were considered simultaneously, the 1 μm particles did not survive for the entire simulation. When inserted in the orbit of Rhea, they survived for only 11 years, while the 100 μm particles remained stable the entire 500-year period. In Figure 5.9a), we observe that the particle's eccentricity had already reached 1, resulting in a highly elongated orbit, after which the subsequent results ceased to have physical meaning.

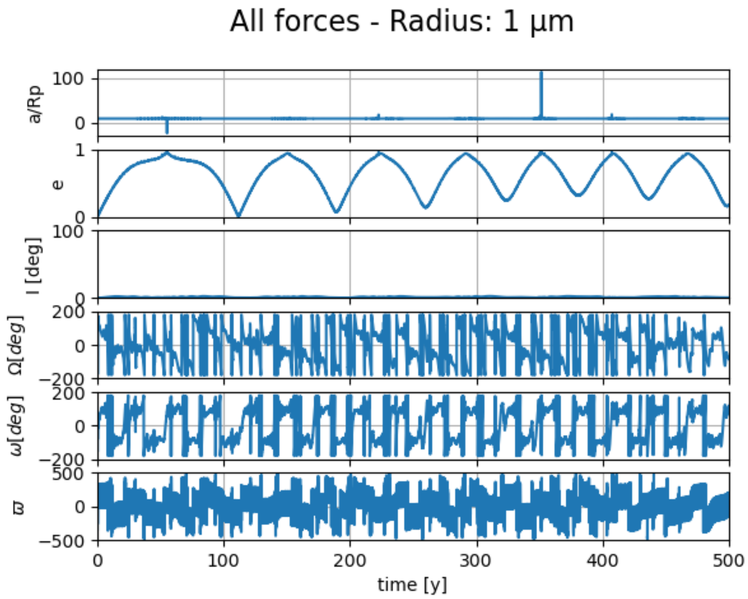

(a)

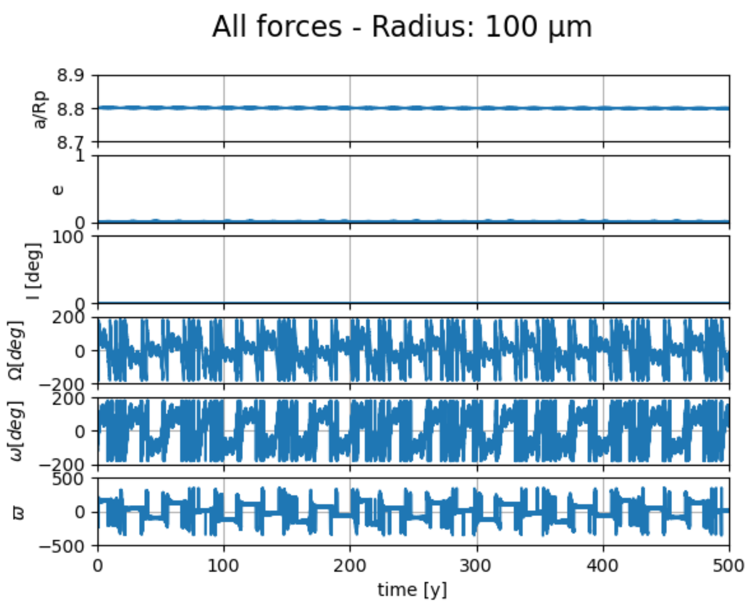

(b)

Figure 5.9: Combined impact of planetary oblateness forces, electromagnetic forces, solar radiation, and plasma drag on the orbits of particles with sizes of (a) 1 μm and (b) 100 μm, initially inserted into the orbits of Rhea (8.8 R_s), over 500 years of integration.

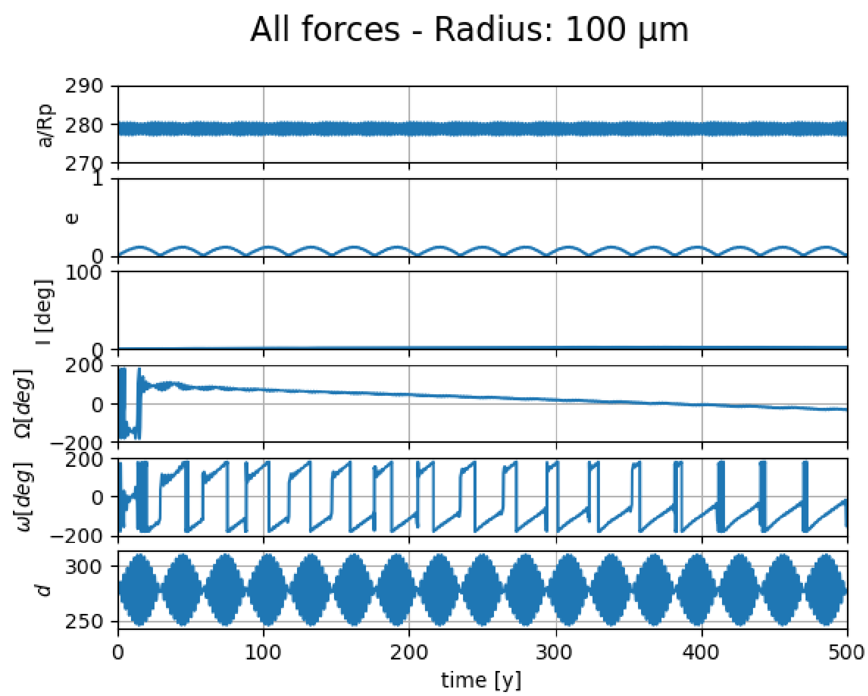

Figure 5.10: Combined impact of planetary oblateness forces, electromagnetic forces, solar radiation, and plasma drag on the orbits of particles with sizes of (a) 1 μm and (b) 100 μm, initially inserted into the orbits of Siarnaq (278 R_s), over 500 years of integration.

5.2 Orbital evolution of particles in Saturn's families.

In this section, we analyze the evolution of the particles with different initial conditions, considering three particle sizes (1 μm, 10 μm, and 100 μm) associated with different families. The particles were inserted into the regions corresponding to each family, according to the intervals described in Table 2.1, and were simulated over a period of 3500 years. The main objective was to examine the behavior of the particles within these regions and identify their possible fates.

From this point onward, the orbital radius (d) is also shown in the plots, representing the instantaneous distance between the dust particle and the central body along its orbital trajectory. This parameter is not independent, as it is determined by the semi-major axis, the orbital eccentricity, and the particle's position along the orbit.

Analyzing the results obtained for the Gallic family (Figue 5.11), we observed that all 1 μm particles were ejected within 1.1 years. In contrast, the 10 μm and 100 μm particles survived throughout the entire simulation time (3500 years).

We examine the particles inserted into the region of the Inuit family (Figure 5.12). The results show that all 1 μm particles were ejected after 1.35 years, while the 10 μm and 100 μm particles survived for the full integration period (3500 years).

Finally, in the Norse family (Figure 5.13), we observed that the particles included in this region experience a strong influence from the perturbative forces: all 1 μm particles were ejected almost immediately (1.65 years), 4 of the 10 μm particles were also ejected after 1951 years, and all 100 μm particles survived for the entire 3500 years. It is apparent that variations in eccentricity have a significant impact on the behavior of the semi-major axis, generating oscillations in its magnitude over time. As the eccentricity approaches values close to 1, the system exhibits pronounced peaks in the semi-major axis.

From the analysis of Figures 5.11–5.13, we observe that the influence of the perturbative forces on the particle orbits increases with distance from the planet. This occurs mainly due to the contribution of radiation pressure, since the farther a particle is from the planet, the gravitational influence decreases, reducing the competition between solar radiation pressure and gravity.

With increasing particle radius, the influence of the forces on the orbital elements decreased, as expected, given that the solar radiation force is inversely proportional to particle size. The 1-micrometer particles were ejected from the system the moment we started the simulation. This information shows that 1-micrometer particles would not survive in the Norse, Gallic, and Inuit regions, as they are strongly influenced by perturbative forces.

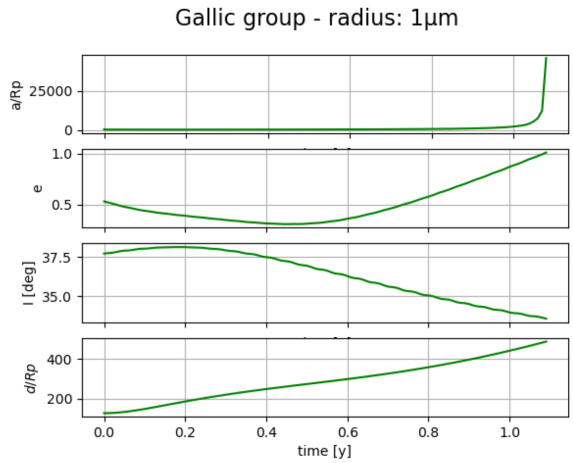

(a)

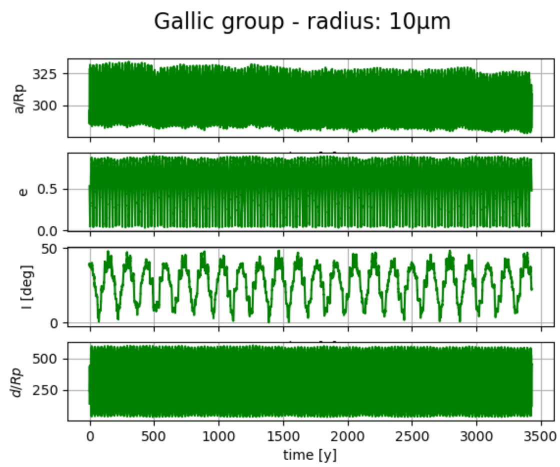

(b)

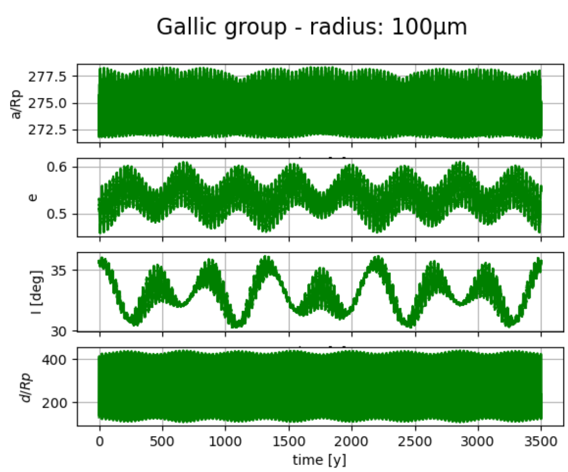

c)

Figure 5.11: Orbital evolution of Gallic family particles for different particle sizes (a) 1 μm, (b) 10 μm, (c) 100 μm.

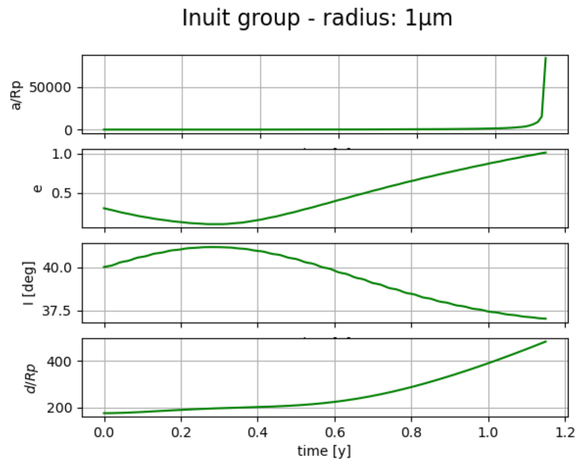

(a)

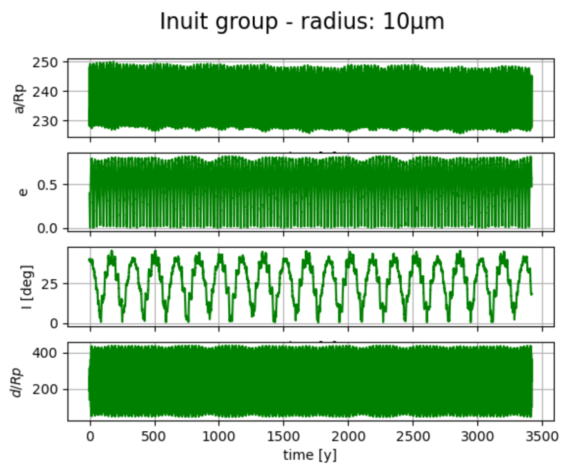

(b)

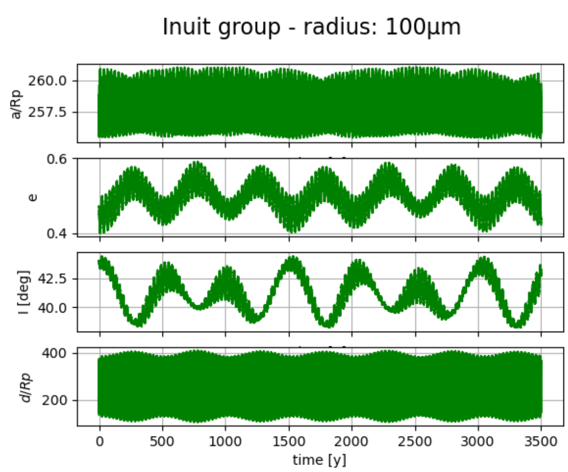

c)

Figure 5.12: Orbital evolution of Inuit family particles for different particle sizes: (a) 1 μm, (b) 10 μm, (c) 100 μm.

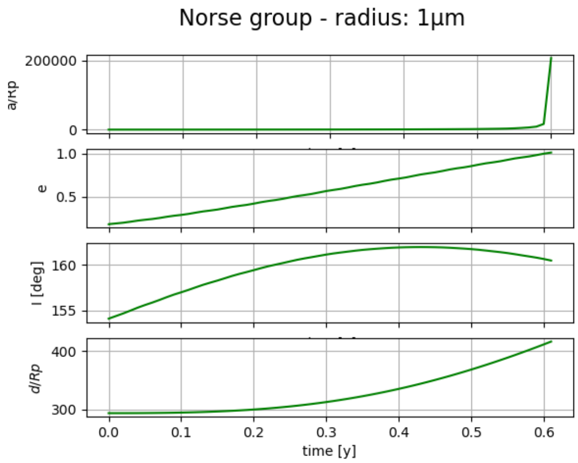

(a)

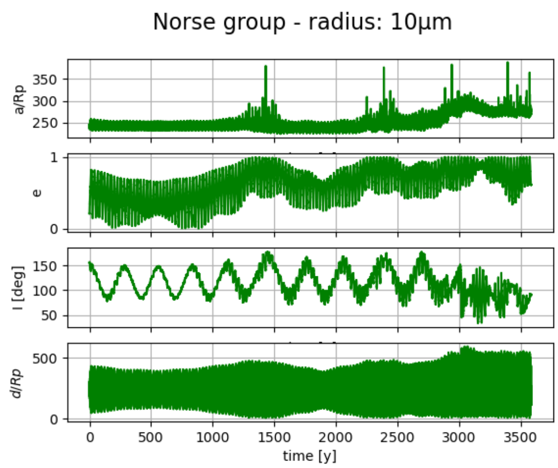

(b)

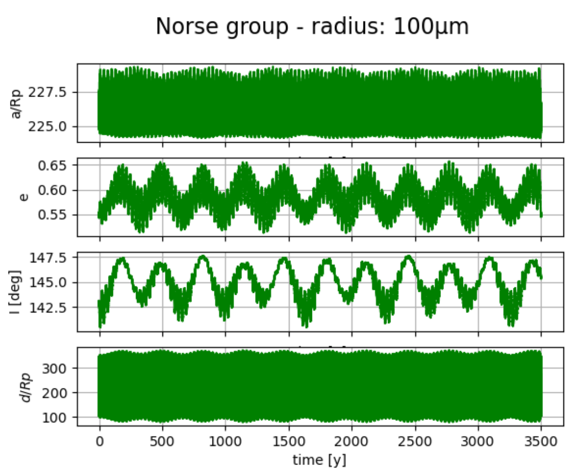

(c)

Figure 5.13: Orbital evolution of Norse family particles for different particle sizes: (a) 1 μm, (b) 10 μm, (c) 100 μm.

5.3 Dust production rates from Saturn's satellite system

We also calculated the amount of material ejected from all of Saturn's satellites, and these values are presented in the last columns of Tables A.1–A.5. These results allow a comparative analysis of dust production throughout the satellite system and provide information on the main physical mechanisms controlling ejecta generation. In our calculations, we considered a typical impactor with $m_{imp} = 10^{-8} kg$, $r \approx 100\mu m$, and $v_{imp} = 23 km/s$.

We analyzed the dust production of the largest and smallest satellites in each family. For the Norse family, we considered Ymir (9 km), with $M^+ = 2.92 \times 10^{-6} kg/s$, and Fenrir (2 km), with $M^+ = 1.44 \times 10^{-7} kg/s$. In the Inuit family, we analyzed Siarnaq (16 km), with $M^+ = 9.22 \times 10^{-6} kg/s$, and Tarqeq (3 km), with $M^+ = 3.24 \times 10^{-7} kg/s$. Finally, in the Gallic family, we considered Albiorix (13 km), with $M^+ = 6.09 \times 10^{-6} kg/s$, and Bebhionn (3 km), with $M^+ = 3.24 \times 10^{-7} kg/s$. In all cases, the difference in dust production between the largest and smallest satellites is approximately one order of magnitude, which can be mainly attributed to the difference in their radii.

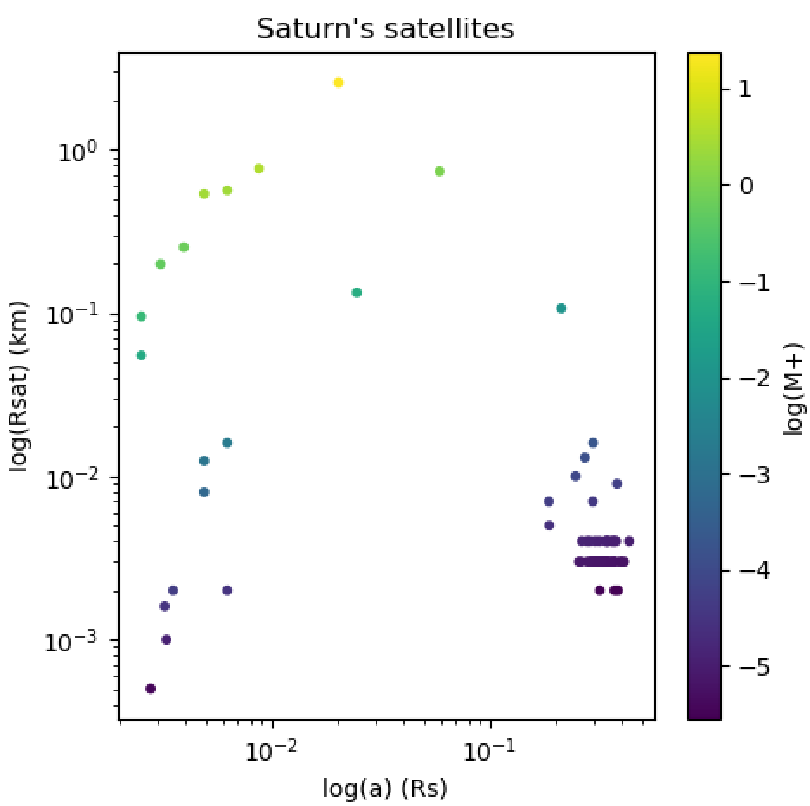

Figure 5.14: Dust production rate for Saturn's moons.

Figure 5.14 shows the dust production rates for Saturn's satellites as a function of their semi-major axis and physical size, with colors indicating the amount of dust produced.

It can be seen that satellites located closer to Saturn produce significantly more dust than distant satellites. This behavior is primarily associated with the effect of gravitational focusing. As interplanetary and intersatellite grains approach the planet, their velocities and spatial densities increase due to Saturn's gravitational field. Consequently, satellites orbiting at smaller planetocentric distances are exposed to a higher flux of faster impactors, resulting in a higher efficiency of ejecta production generated by impacts.

In addition to orbital distance, the satellite radius also influences the dust production rate. Larger satellites present a greater cross-sectional area for impacts, increasing the probability of collisions with incoming grains. As a result, satellites with larger radii generally exhibit higher dust production rates, even when located at comparable orbital distances.

The combined dependence on orbital distance and satellite size suggests that dust production in Saturn's satellite system is controlled by both dynamical and physical properties. Inner satellites benefit from stronger gravitational focusing, while larger satellites present a higher probability of dust production due to their increased impact cross sections.

5.4 Analysis of particle ejection from the satellites

At this stage of the work, we selected one satellite from each family and performed one simulation for each case, ejecting 100 particles from each satellite in order to track their trajectories under the influence of perturbative forces over time. The particles were isotropically ejected from the satellite's equator, at a distance corresponding to 1% of the planet's radius, with the velocity given by expression 4.1. We simulated the entire system over a time interval of 5000 years.

For the Norse family, we selected the satellite Ymir; for the Gallic family, Albiorix; and for the Inuit family, Siarnaq. The physical and orbital parameters of the satellites considered are listed in Table 5.1. These satellites were selected because they are the largest members of their respective families, except for the Norse family, for which we selected the second-largest satellite.

Table 5.1: Parameters of the selected satellites.

Satellite	**a (R_S)**	**e**	**i (°)**	**Mass (kg)**	**Radius (km)**
Albiorix	273.50	0.54	3.96×10^{1}	22.3×1015	13
Ymir	384.55	0.36	1.47×10^{2}	3.97×10^{15}	9
Siarnaq	298.36	0.51	6.34×10^{1}	43.5×10^{15}	16

Source: Sheppard (2019)

The resulting trajectories of particles ejected from Siarnaq are shown in Figure 5.15. Among the 100 simulated particles, we identify three distinct outcomes: ejection from the system, collision with the planet, and long-term survival within the system. Representative examples of each case are illustrated in Figure 5.15. Panel (a) shows a particle that is ejected from the system after approximately 800 years, when its eccentricity reaches unity. Panel (b) presents a particle that collides with the planet after about 3000 years. Finally, panel (c) corresponds to a particle that survives throughout the entire integration time.

In all plots of Figure 5.15, we observe that when a particle's eccentricity approaches 1, its orbital evolution is strongly affected, showing pronounced peaks in the semi-major axis and significant variations in inclination. This occurs because, for eccentricities close to 1, the particle approaches very close to the planet at pericenter, experiencing a strong gravitational interaction that modifies its orbital elements.

Analyzing the behavior of the surviving particles, we observed that they are transported to more distant regions of the planet. Over time, these particles move away from the region associated with their original family and migrate away from the system.

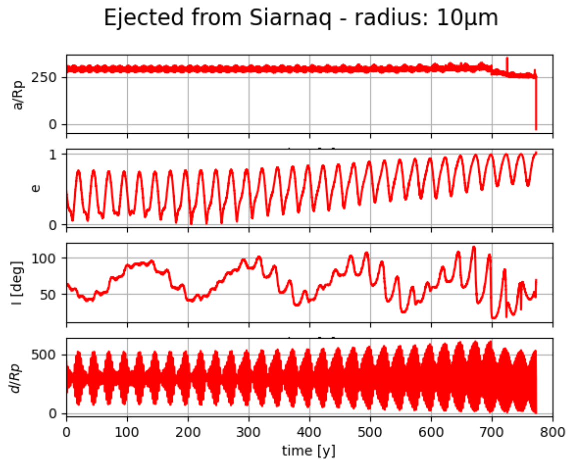

(a) System ejection

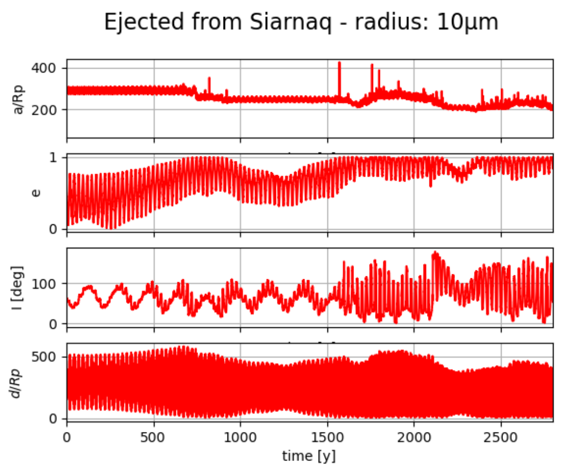

(b) Collision with the planet

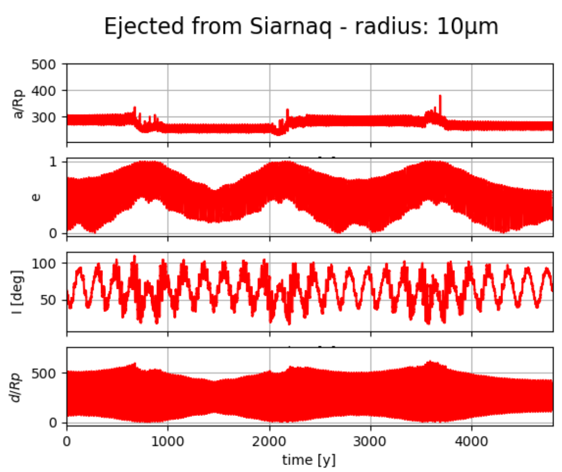

(c) Survivor

Figure 5.15: Orbital evolution of 10 μm particles ejected from the Siarnaq satellite. Each panel shows a different outcome.

For the satellite Ymir, 24 of the 100 ejected particles were ejected from the system, while the remaining 76 remained stable throughout the simulation. The corresponding results are shown in Figure 5.16.

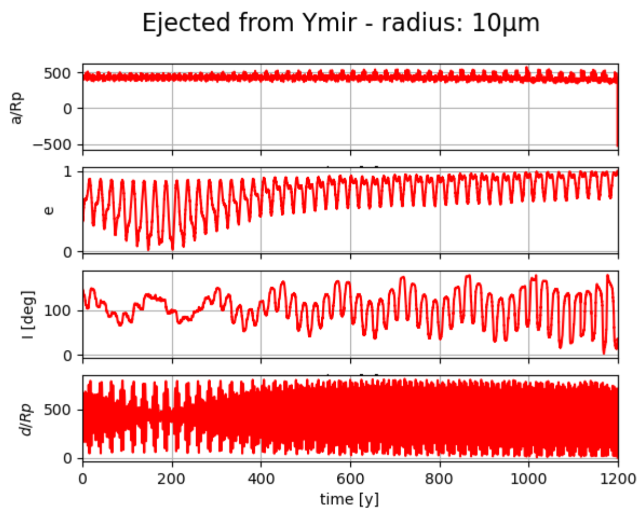

(a) System ejection

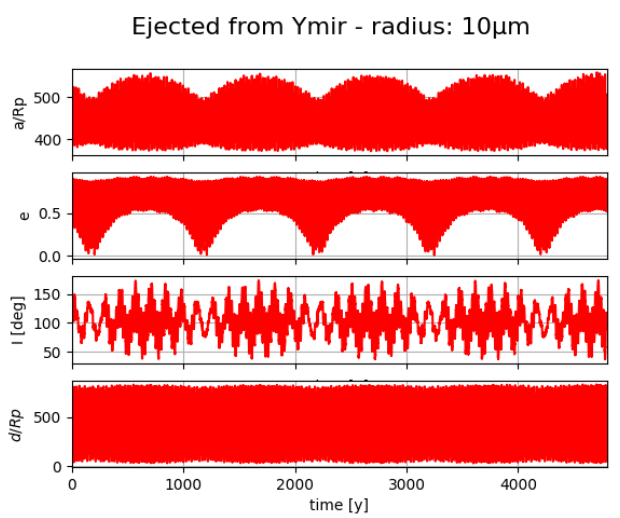

(b) Survivor

Figure 5.16: Orbital evolution of 10 μm particles ejected from the Ymir satellite. Each panel shows a different outcome.

In Figure 5.16a), the particle's behavior is similar to that shown in Figure 5.15a) As the eccentricity increases and approaches 1, both the semi-major axis and the inclination exhibit large variations. Once the eccentricity reaches 1, the particle is ejected from the system.

For Albiorix, all ejected particles remained stable throughout the 5000-year interval, with no evidence of either system ejection or collision with the planet, as illustrated in Figure

5.17.

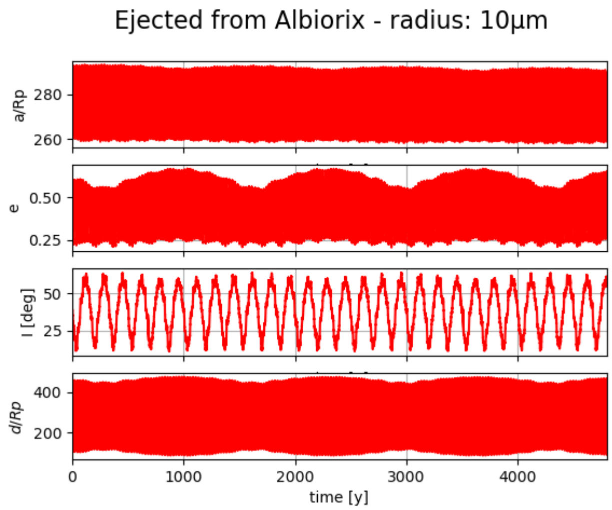

Figure 5.17: Orbital evolution of 10 μm particles ejected from the Albiorix satellite.

We analyzed the simulation data and determined the number of particles corresponding to each possible outcome: those that collided with satellites, those that impacted the planet, those ejected from the system, and the surviving particles. All cases are summarized in Table 5.2.

Satellites	**Total particles**	**System ejection**	**Collision with the planet**	**Collision with the satellites**	**Survivor**
Siarnaq	100	38%	3%	0%	59%
Ymir	100	0%	0%	0%	100%
Albiorix	100	24%	0%	0%	76%

Table 5.2: Percentage of particles in different fates.

The data in Table 5.2 indicate that particles associated with different families exhibit distinct dynamical outcomes. We observe a general tendency for particles to be ejected from the system once they transition to hyperbolic orbits. No collisions with satellites were detected in any of the simulations, while collisions with the planet occurred only for particles originating from the vicinity of Siarnaq.

The particles ejected from the satellite closest to the planet presented higher initial eccentricities, but were the least dynamically affected throughout the simulation, such that none of them were ejected from the system. In contrast, particles launched from satellites farther from the planet, originating from Siarnaq and exhibiting high eccentricities, experienced stronger perturbations, resulting in both ejections from the system and collisions with the planet. In the case of the particles associated with the most distant satellite, Ymir, with an initial eccentricity of 0.4, significant variations in the particles' orbit occurred, resulting to the ejection of particles from the system. These results suggest that the fate of the particles is strongly influenced by their satellite of origin, highlighting the relationship between particle dynamics and the orbital characteristics of the source satellites.

5.5 Particle trajectory

After analyzing the action of perturbative forces on particle dynamics, as well as the differences associated with particle size and ejection distance, we performed the final simulation of the system. At this stage, we considered the planet, 15 satellites, and 50 particles with radii of 1 μm and 10 μm, including all relevant forces. Only satellites with radii larger than 10 km were included, since smaller bodies did not cause a significant gravitational influence on the orbital dynamics of the dust particles.

In this stage, we performed the same analysis of the orbital elements for both particle sizes in order to verify the consistency of the results. As expected, the 1 μm particles were rapidly ejected from the system (see Figure 5.18), while the 10 μm particles remained in orbit for longer periods (see Figure 5.19).

We also analyzed the density distribution of the ejected particles in each region, illustrated in Figure 5.20, Figure 5.21, and Figure 5.22. In these plots, individual trajectories are shown in shades of gray, such that darker regions correspond to ranges of orbital elements where particles spend more time throughout the integration, while lighter areas indicate that fewer particles reach those values. This representation allows for direct visualization of the regions where particles spend most of their time and the preferred trajectories of particles within the system.

Particles ejected from the Norse family initially exhibit orbital elements that are strongly concentrated within the characteristic region of this population, as evidenced by the darker areas in the semi-major axis, eccentricity, and inclination plots. However, with the evolution of the integration, a dispersion of these elements is observed, resulting in an increasingly diffuse and less dense distribution over time. This behavior indicates that, although the particles preserve the orbital characteristics of their source family for some time, gravitational perturbations and dissipative effects—such as Poynting–Robertson drag—promote their migration into regions associated with other families. Therefore, the results demonstrate that particles can transition between different dynamical regions of the system independent of their family of origin, highlighting the efficiency of transport across families during orbital evolution.

Particles ejected from the Inuit family exhibit a more stable behavior. As shown in Figure

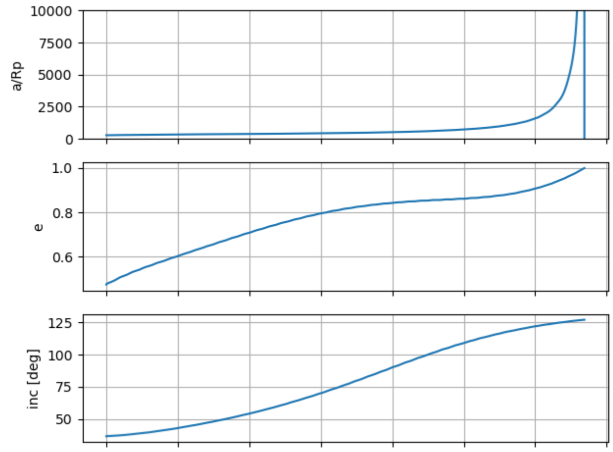

(a) Particles ejected from Albiorix

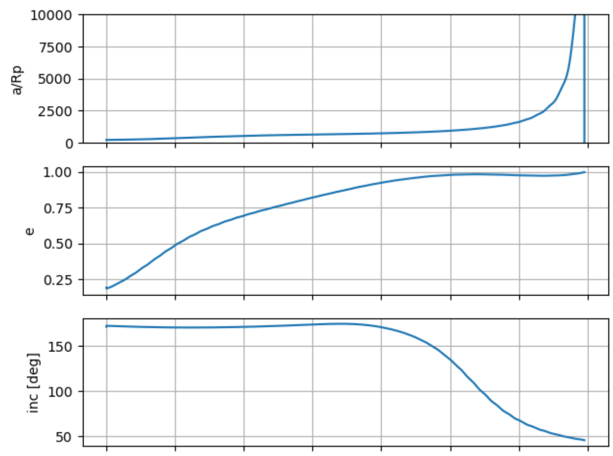

(b) Particles ejected from Phoebe

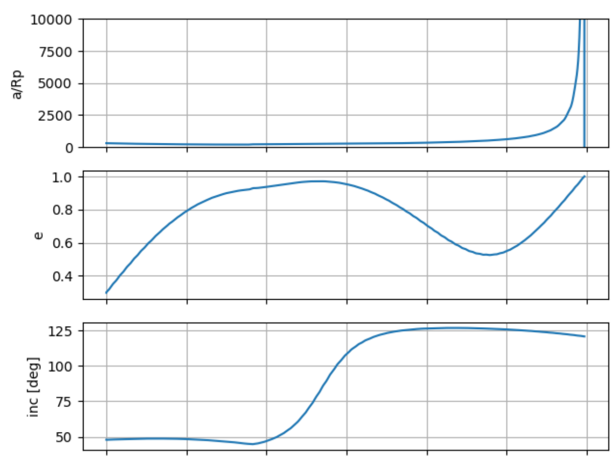

(c) Particles ejected from Siarnaq

Figure 5.18: Orbital evolution of 1 μm particles ejected from satellites.

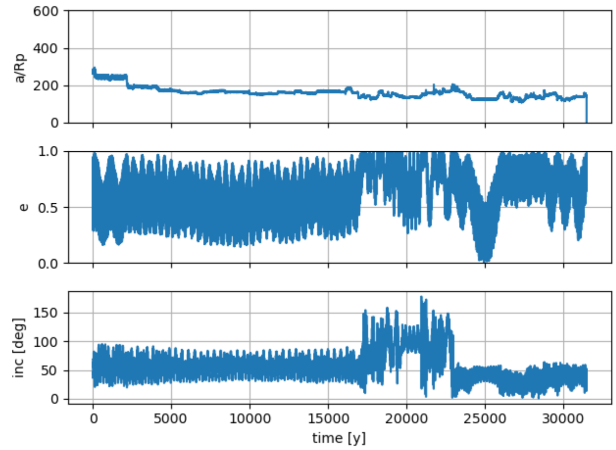

(a) Particles ejected from Albiorix

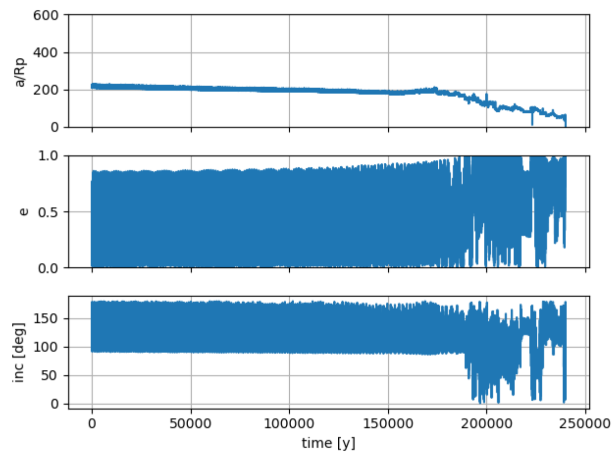

(b) Particles ejected from Phoebe

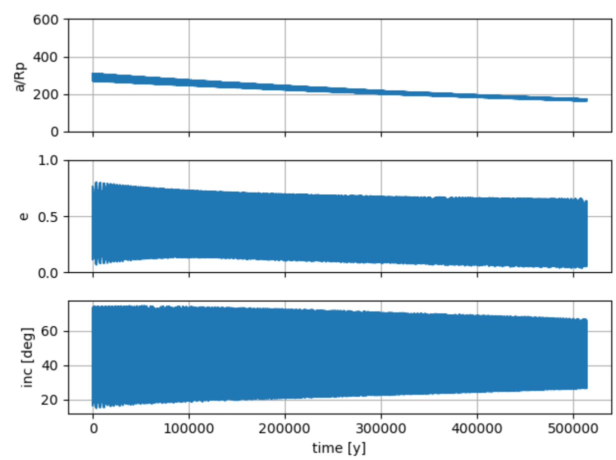

(c) Particles ejected from Siarnaq

Figure 5.19: Orbital evolution of 10 μm particles ejected from satellites.

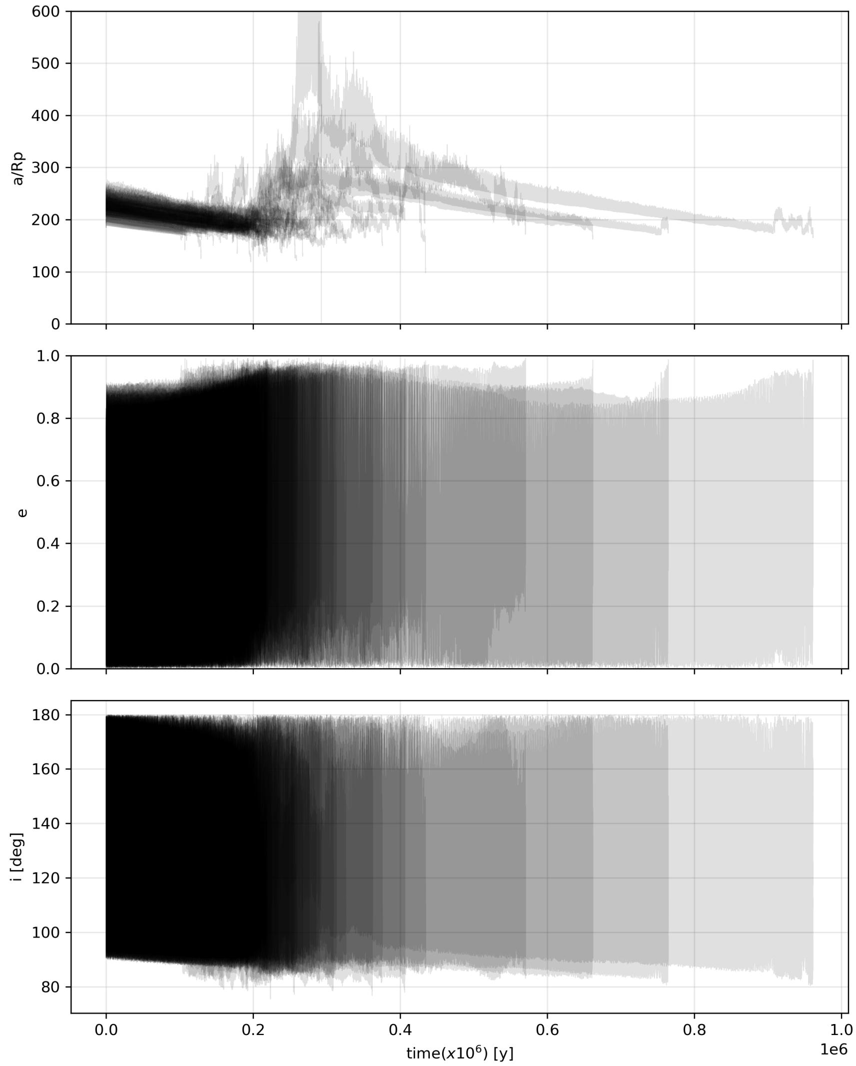

Figure 5.20: Density distribution of ejected particles from the Norse family.

5.21, the ejected particles follow similar trajectories, preserving the orbital characteristics typical of their source family over long periods. In contrast to particles from more dynamically disturbed families, such as the Norse family, those originating from the Inuit family exhibit only limited dispersion over time, indicating that external gravitational perturbations exert less influence on their trajectory. Only dissipative effects, such as Poynting-Robertson drag, dominate their evolution, transporting the particles to more internal orbits.

Particles ejected from the Gallic family show an orbital evolution characterized by two distinct phases. During the first 300 kyr, a strongly perturbed regime is observed, characterized by substantial dispersion in semi-major axis, eccentricity, and inclination, indicating intense gravitational interactions and a quick alteration of the original orbital properties. After this initial chaotic phase, the dynamics become more regular and are predominantly

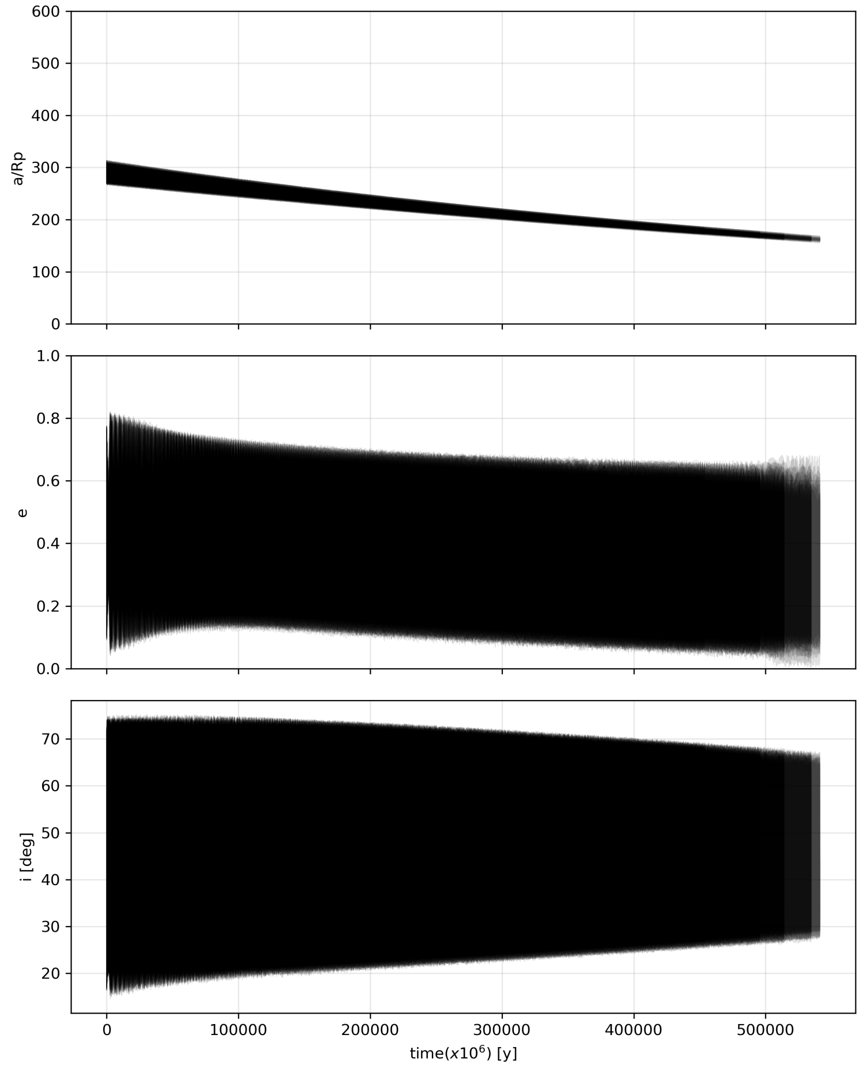

Figure 5.21: Density distribution of ejected particles from the Inuit family.

governed by dissipative effects, which gradually transport the particles toward more inner orbits.

Subsequently, we analyzed the trajectories of the particles with respect to the regions of the satellite families, based on the orbital elements (a, e, i). The regions corresponding to each family were defined using the pericenter and apocenter values of their respective satellites. To represent these regions in orbital space, we applied the convex hull method to construct polygons delimiting each group.

At this stage, in all simulated cases, the particles exhibited two possible outcomes: they either survived throughout the entire simulation period, migrating between different regions, or were ejected from the system when the eccentricity reached 1. We quantified both the number of particles that remained in the system and those that were ejected, as well as the

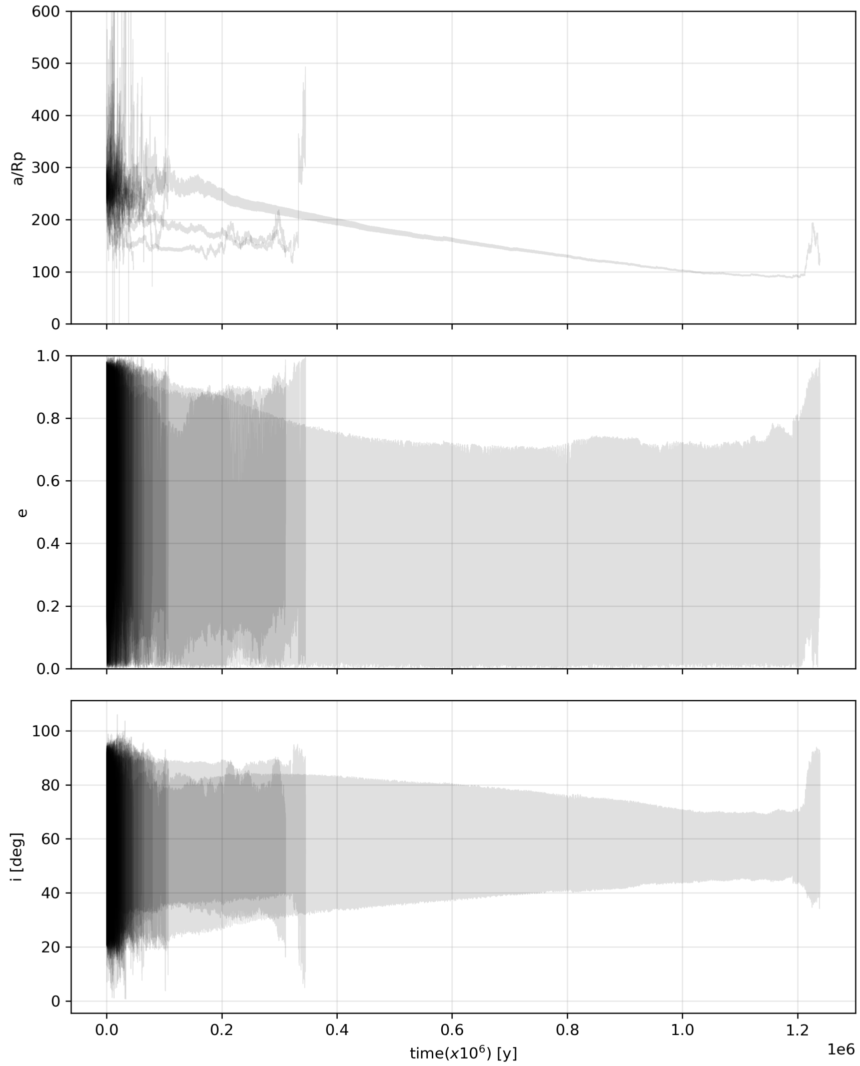

Figure 5.22: Density distribution of ejected particles from the Gallic family.

average lifetime of the particles ejected from each family. These statistics are presented in Table 5.3.

Particles with a radius of 1 μm were ejected from the system in approximately 5 to 6 years. This behavior results from the action of Poynting–Robertson drag, which strongly affects their orbits, as illustrated in Figure 3.3.

A different dynamical behavior was observed for particles with a radius of 10 μm. Particles ejected from the Gallic family survived for approximately 1286733 years, while those ejected from the Norse family had lifetimes of around 995616 years. Particles ejected from the Inuit family, however, remained stable throughout the entire simulation period.

During the simulations, we observed that particles with a radius of 10 μm ejected from Albiorix exhibited significant variations in their orbital elements (a, e), as illustrated in Figure

Table 5.3: Percentage of ejected and surviving particles for different sizes of dust grains originating from three irregular satellites (Albiorix, Siarnaq and Phoebe), with the time corresponding to the ejection of the last particle.

Particle radius	**Source body**	**Ejected particles**	**Surviving particles**	**Time (years)**
1 μm	Albiorix	100%	0%	5
10 μm	Albiorix	100%	0%	1286733
1 μm	Siarnaq	100%	0%	6
10 μm	Siarnaq	0%	100%	757197
1 μm	Phoebe	100%	0%	5
10 μm	Phoebe	100%	0%	995616

5.23 a) and (a, i) as illustrated in Figure 5.23 b). The analyzed trajectory (shown in black) begins within the region associated with the Gallic family (in red) and, over the course of its evolution, is also transported to regions corresponding to the Inuit and Norse families. This behavior suggests that non-gravitational forces, together with the gravitational perturbations of Saturn and its satellites, exert a strong influence on the transport of particles between different families, facilitating material exchange within the system. In the specific case analyzed, the particle remained for approximately 125 years in the Gallic family, 1427 years in the Inuit family, 32 years in the Norse family, and 29882 years outside the family regions.

In the case of particles ejected from the Inuit family, illustrated in Figure 5.23 c) and Figure 5.23 d), a behavior similar to that of the particle originating from the Gallic family is observed, although, the particle trajectory remains more confined between the Inuit and Gallic regions. The analyzed trajectory begins in the Inuit family region (green) and, during its evolution, also crosses the region associated with the Gallic family. Specifically, the particle remained for approximately 9167 years in the Gallic family, 57324 years in the Inuit family, and 447437 years outside the family regions.

In the case of a particle originating from the Norse family, a more perturbed orbital evolution is observed, as illustrated in Figure 5.23 e) and Figure 5.23 f). Although the semimajor axis gradually decreases due to Poynting–Robertson drag, transporting the particle toward more inner orbits, the most notable feature is the pronounced variation in inclination. In the analyzed case, the particle remained for approximately 41686 years in the Norse family, 13 years in the Inuit family, 1 year in the Gallic family, and 194680 years outside the family regions. Extending the analysis to all simulated particles, we identified several cases in which fragments ejected from Phoebe reach the dynamical regions of the Gallic and Inuit families, demonstrating that material originating from the Norse family can be efficiently transported throughout the system and contaminate other satellite populations.

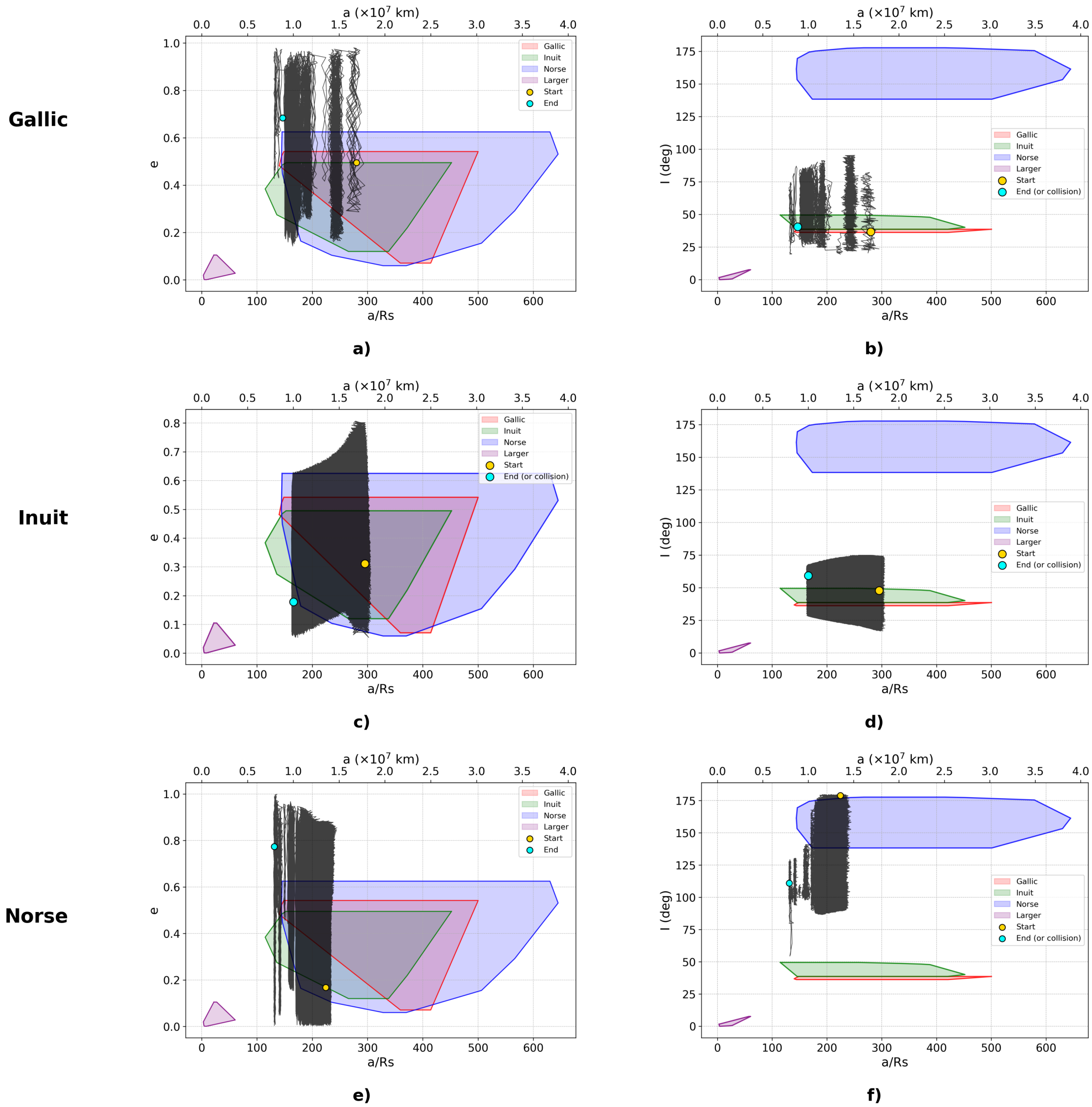

Figure 5.23: Orbital evolution of the last surviving particles with a radius of 10 μm, ejected from Saturn's families.

5.6 Albedo analysis

Albedo is an important photometric property used in the classification of planetary surfaces and small bodies in the Solar System. It represents the fraction of solar radiation reflected by an object: values close to 0 indicate dark, poorly reflective surfaces, while values near 1 correspond to highly bright bodies. This parameter provides important information about a body's composition and surface characteristics. In natural satellites, variations in albedo can reveal geological remodeling processes, such as volcanism or erosion, as well as external phenomena, such as the deposition of material originating from other populations. Therefore, studying albedo is crucial for understanding surface evolution, the interactions between satellites and their environments, and the mechanisms of material transport within the planetary system.

Saturn's satellites exhibit a wide range of albedo values (see Table 5.4), covering more than two orders of magnitude, from very dark objects such as Albiorix and Siarnaq to highly reflective bodies such as Enceladus and Tethys. This broad distribution reflects the combined influence of intrinsic surface properties, collisional processes, and external dust transport acting throughout the Saturnian system.

Satellites	**Albedo**	**Radius (km)**
Mimas	0.8	198.5
Enceladus	1	294.5
Tethys	0.8	530
Dione	0.55	559
Rhea	0.65	764
Titan	0.21	2575
Hyperion	0.47	133
Iapetus	0.02-0.05/0.5-0.6	718
Phoebe	0.10	120
Telesto	0.5	12
Janus	0.70	89
Epimetheus	0.70	59.5
Albiorix	0.06	16
Paaliaq	0.06	11
Siarnaq	0.05	20

Table 5.4: Albedo of Saturn's satellites.

.

Among the regular satellites, albedo values tend to be significantly higher, typically ranging from 0.2 to 1.0. These elevated values are consistent with surfaces dominated by water ice and active resurfacing processes, such as cryovolcanism and endogenic activity, particularly in the case of Enceladus. In contrast, the irregular satellites display systematically lower albedo values, generally between 0.05 and 0.06, indicating dark, primitive surfaces that have experienced limited internal processing.

Although the Gallic, Inuit, and Norse families have different origins, they exhibit similar albedo distributions. This similarity cannot be explained solely by their primitive composition and instead suggests the presence of continuous dust exchange among these populations. Micrometeoroid impacts generate dust particles that are subsequently redistributed by radiation forces and gravitational perturbations, promoting the homogenization of surface reflectivities across families. This same material slowly migrates inward through the system under the action of Poynting–Robertson drag, depositing dust on the surfaces of inner satellites, such as Iapetus (Tosi et al. 2010), consequently modifying their albedos and recording the dynamical influence of the irregular populations.

As a result, the observed photometric properties do not exclusively reflect the intrinsic characteristics of each family, but instead arise from an active process of material exchange that dynamically connects all satellite groups throughout the Saturnian system.

The similarity in albedo, combined with the analysis of particle trajectories, indicates that dust particles, independent of their family of origin, can migrate to other families, highlighting efficient transport across all regions of the system.

Chapter 6

Final remarks

In this work, we investigate the production and evolution of dust particles in the Saturnian system, exploring the mechanisms responsible for their generation and the perturbative forces that shape their orbits. To this end, we track the dynamics of particles ejected from Saturn's satellites in order to determine if the material remains in the region associated with its family of origin or migrates to other areas of the system.

We developed a code based on the IAS15 integrator of the REBOUND package, which enables high-precision simulations of the orbital evolution of the particles, from their ejection from the satellites to collisions with the planet or satellites, or eventual ejection from the system.

The results demonstrated that perturbative forces, such as planetary oblateness, electromagnetic forces, solar radiation, and plasma drag, exert different influences depending on the size and location of the particles. While particles with smaller radii are strongly affected by non-gravitational forces and are rapidly removed from the system, larger particles exhibit greater stability, with trajectories dominated by the gravitational effects of Saturn and its satellites. In addition, the dust production rates calculated for different satellite groups revealed significant variations, directly related to the size and location of the bodies within the system.

We also observed that orbital perturbations eject a large fraction of the particles, mainly as a consequence of their high eccentricities. However, we identified a smaller fraction that survives throughout the entire simulation time, with the potential to migrate to more inner regions and collide with the planet.

The results indicate that the fate of the particles is closely related to the orbital characteristics of their parent satellites. Satellites closer to the planet are more likely to provide greater stability to the ejected particles, while those on more distant orbits, especially when associated with high eccentricities, promote perturbations that can lead to ejection from the system or collisions with the planet.

In addition, the results indicate that perturbative forces modify the orbital elements of the particles, promoting migration between families. Particles ejected from the Gallic and Inuit families exhibit frequent material exchange between them, mainly due to the spatial proximity of their regions. This suggests that dust grains ejected from the Gallic family can occupy the region associated with the Inuit family. In contrast, particles from the Norse family exhibit a more restricted migration pattern, remaining confined to their own region; however, a fraction of the particles also reaches the Inuit and Gallic regions.

This migration pattern is directly related to the albedo properties observed in the irregular satellites. The Gallic, Inuit, and Norse families exhibit similarly low albedo values, indicating that these characteristics are not determined exclusively by the original composition of each family but also by a continuous process of material exchange. The migration of particles between regions, as evidenced by the simulations, promotes the mixing of dust among the families and contributes to the homogenization of their surfaces. Therefore, the combined dynamical and photometric results demonstrate that material transport has a strong influence on surface evolution and promotes interactions among Saturn's irregular satellite populations.

This study contributes to the understanding of the mechanisms responsible for the generation and evolution of dust particles in planetary systems and allows an investigation of the migration behavior among the different satellite families. The methods employed and the results obtained provide useful support for future investigations of similar systems, such as Jupiter's, and allow for improvements to models that include additional forces or different initial conditions.

Bibliography

ASHTON, E., GLADMAN, B., ALEXANDERSEN, M., & PETIT, J.-M. Discovery of 128 new saturnian irregular moons. *Research Notes of the AAS*, 9(3):57, 2025.

BURNS, J. A., HAMILTON, D. P., & SHOWALTER, M. R. Dusty rings and circumplanetary dust: Observations and simple physics. *Astronomy and Astrophysics Library*, 101:641–725, 2001.

BURNS, J. A., LAMY, P. L., & SOTER, S. Radiation forces on small particles in the solar system. *Icarus*, 40:1–48, 1979.

CAMPBELL, J. & ANDERSON, J. Gravity field of the saturnian system from pioneer and voyager tracking data. *The astronomical jornal*, 97(5), 1989.

COLOMBO, G., SHAPIRO, I. I., & LAUTMAN, D. A. The Earth's Dust Belt: Fact or Fiction?, 3, Lunar Ejecta. , 71:5719, 1966.

COLWELL, J. E. & ESPOSITO, L. W. A numerical model of the uranian dust rings. *Icarus*, 86(2):530–560, 1990.

DANBY, J. M. A. *Fundamentals of celestial mechanics*. 1988.

DIKAREV, V., GRÜN, E., BAGGALEY, J., GALLIGAN, D., LANDGRAF, M., & JEHN, R. The new esa meteoroid model. *Advances in Space Research*, 35(7):1282–1289, 2005. Space Debris.

DOUGHERTY, M. K., CAO, H., KHURANA, K. K., HUNT, G. J., PROVAN, G., KELLOCK, S., BURTON, M. E., BURK, T. A., BUNCE, E. J., COWLEY, S. W. H., & MARGARET G. KIVELSON, D. J. S., CHRISTOPHER T. RUSSELL. Saturn's magnetic field revealed by the cassini grand finale. *Science*, 362, 2018.

GLADMAN, J., KAVELAARS, J., HOLMAN, M., NICHOLSON, P., BURNS, J., HERGENROTHER, C., PETIT, J.-M., MARSDEN, B., JACOBSON, R., GRAY, W., & GRAV, T. Discovery of 12 satellites of saturn exhibiting orbital clustering. *Nature*, 412:163–6, 2001.

GRESHKO, M. National geographic. 2019.

GRÜN, E., ZOOK, H., FECHTIG, H., & GIESE, R. Collisional balance of the meteoritic complex. *Icarus*, 62(2):244–272, 1985.

Hamilton, D. P. Motion of dust in a planetary magnetosphere - orbit-averaged equations for oblateness, electromagnetic, and radiation forces with application to saturn's e ring. *Icarus*, 101:244–264, 1993.

Hamilton, D. P. & Krivov, A. V. Circumplanetary dust dynamics: Effects of solar gravity, radiation pressure, planetary oblateness, and electromagnetism. *Icarus*, 123(2):503–523, 1996.

Horanyi, M., Burns, J. A., & Hamilton, D. P. The dynamics of saturn's e ring particles. *Icarus*, 97(2):248–259, 1992.

Krivov, A. V., Sremčević, M., Spahn, F., Dikarev, V. V., & Kholshevnikov, K. V. Impact-generated dust clouds around planetary satellites: spherically symmetric case. , 51(3):251–269, 2003.

Kuga, H. K., Rao, K. R., & Carrara, V. *Satélites Artificiais–Movimento Orbital*. 2011.

Landgraf, M., Liou, J.-C., Zook, H. A., & Grün, E. Origins of solar system dust beyond jupiter. *The Astronomical Journal*, 123(5):2857–2861, 2002.

Madeira, G., Sfair, R., Mourão, D. C., & Giuliatti Winter, S. M. Production and fate of the g ring arc particles due to aegaeon (saturn liii). *Monthly Notices of the Royal Astronomical Society*, 475(4):5474–5479, 2018.

Mignard, F. Effects of radiation forces on dust particles in planetary rings. *GREENBERG, R. and BRAHIC, A.*, page 333–366, 1984.

Morfill, G., Grun, E., & Johnson, T. Dust in jupiter's magnetosphere physical processes. *Planetary and Space Science*, 28(12):1087–1100, 1980.

Nesvorný, D., Alvarellos, J. L. A., Dones, L., & Levison, H. F. Orbital and collisional evolution of the irregular satellites. *The Astronomical Journal*, 126(1):398, 2003.

Nesvorný, D., Jenniskens, P., Levison, H. F., Bottke, W. F., Vokrouhlický, D., & Gounelle, M. Cometary origin of the zodiacal cloud and carbonaceous micrometeorites. implications for hot debris disks. *The Astrophysical Journal*, 713(2):816–836, 2010.

Nesvorný, D., Vokrouhlický, D., & Morbidelli, A. Capture of irregular satellites during planetary encounters. *The Astronomical Journal*, 133(5):1962, 2007.

Persan, A. Astrônomos descobrem 62 novas luas em saturno; número ultrapassa as de júpiter. 2023.

Poppe, A. & Horányi, M. The effect of nix and hydra on the putative pluto–charon dust cloud. *Planetary and Space Science*, 59(13):1647–1653, 2011. Exploring Phobos.

Poppe, A. R. An improved model for interplanetary dust fluxes in the outer Solar System. , 264:369–386, 2016.

Porter, S. B., Desch, S. J., & Cook, J. C. Micrometeorite impact annealing of ice in the outer solar system. *Icarus*, 208(1):492–498, 2010.

Rein, H. & Spiegel, D. S. Ias15: a fast, adaptive, high-order integrator for gravitational dynamics, accurate to machine precision over a billion orbits. *Monthly Notices of the Royal Astronomical Society*, 446(2):1424–1437, 2015.

Schaffer, L. & Burns, J. A. Lorentz resonances and the vertical structure of dusty rings: Analytical and numerical results. *Icarus*, 96:65–84, 1992.

Sfair, R. & Giuliatti Winter, S. M. The role of Mab as a source for the μ ring of Uranus. , 543:A17, 2012.

Sheppard, S. S. Saturn moons. 2019.

Sheppard, S. S. & Jewitt, D. C. An abundant population of small irregular satellites around saturn. *Nature*, 423:261–263, 2003.

Siqueira, P. B. *Adaptação do integrador Rebound para o estudo de anéis planetários*. Ph.D. thesis, Universidade Estadual Paulista, Faculdade de Engenharia de Guaratinguetá, Guaratinguetá, São Paulo - Brasil, 2019.

Spahn, F., Albers, N., Hörning, M., Kempf, S., Krivov, A. V., Makuch, M., Schmidt, J., Seiss, M., & Miodrag Sremčević. E ring dust sources: Implications from cassini's dust measurements. *Planetary and Space Science*, 54(9):1024–1032, 2006. Physics of Dusty Rings.

Sremčević, M., Krivov, A. V., Krüger, H., & Spahn, F. Impact-generated dust clouds around planetary satellites: model versus galileo data. *Planetary and Space Science*, 53(6):625–641, 2005.

Tosi, F., Turrini, D., Coradini, A., Filacchione, G., & the VIMS Team. Probing the origin of the dark material on iapetus. *Monthly Notices of the Royal Astronomical Society*, 403(3):1113–1130, 2010.

Verbiscer, A. J., Skrutskie, M. F., & Hamilton, D. P. Saturn's largest ring. *Nature*, 461:1098–1100, 2009.

Yeomans, D. K. Horizons web-interface. 2006.

Appendix

Appendix A

Orbital elements of Saturn's satellites

Table A.1: Orbital elements, physical parameters, and dust production of Inuit group satellites discovered before 2019. The values were obtained by the Horizons system, referring to July 16, 2019, and from Sheppard (2019).

Satellites	a ($\times 10^7$) (km)	e ($\times 10^{-1}$)	I (°)	Ω (°)	ω (°)	f (°)	m ($\times 10^{15}$) (kg)	R (km)	M^+ (kg/s)
Kiviuq	1.13	1.56	76.67	217.38	88.34	1.49	2.79	8	5.01e-05
Ijiraq	1.13	3.76	26.47	351.00	9.86	2.91	1.18	6	2.55e-05
Paaliaq	1.50	4.99	70.72	208.48	241.70	14.02	7.25	11	8.79e-05
Siarnaq	1.80	5.08	63.36	258.50	101.70	18.20	43.50	20	2.04e-04
Tarqeq	1.79	1.23	53.43	293.34	103.35	15.81	0.23	3.5	7.20e-06

Source: Yeomans (2006) e Sheppard (2019)

Table A.2: Orbital elements, physical parameters, and dust production of Norse group satellites discovered before 2019. The values were obtained by the Horizons system, referring to July 16, 2019, and from Sheppard (2019).

Satellites	a ($\times 10^7$) (km)	e ($\times 10^{-1}$)	I (°)	Ω (°)	ω (°)	f (°)	m ($\times 10^{15}$) (kg)	R (km)	M^+ (kg/s)
Phoebe	1.29	1.53	152.23	54.81	286.70	44.31	0.83	106.6	1.09-02
Skathi	1.55	2.49	153.80	109.72	166.83	46.31	0.35	4	7.77e-06
Skoll	1.76	4.04	161.27	96.58	129.41	123.26	0.15	3	7.27e-06
Greip	1.82	3.69	159.26	39.51	336.88	175.60	0.15	3	7.14e-06
Hyrrokkin	1.84	3.73	148.64	346.92	338.06	181.03	0.35	4	1.26e-05
Jarnsaxa	1.95	2.11	161.31	6.24	349.89	217.14	0.15	3	6.88e-06
Mundilfari	1.86	1.78	147.57	21.35	20.72	251.79	0.23	3.5	7.06e-06
Narvi	1.91	3.21	109.35	56.41	180.16	164.61	0.23	3.5	6.95e-06
Bergelmir	1.94	1.34	135.16	66.56	123.42	333.31	0.15	3	6.90e-06
Suttungr	1.93	1.15	151.74	52.27	350.57	315.40	0.23	3.5	6.91e-06
Hati	1.97	3.17	167.31	60.15	248.87	149.83	0.15	3	6.84e-06
Bestla	2.04	7.06	166.56	158.25	73.48	156.88	0.23	3.5	6.72e-06
Farbauti	2.00	2.17	128.84	34.26	5.12	148.80	0.09	2.5	6.78e-06
Thrymr	2.04	4.75	152.17	52.03	19.12	186.70	0.23	3.5	6.73e-06
Aegir	2.10	2.07	140.98	52.84	247.21	167.24	0.15	3	6.63e-06
Kari	2.25	3.37	156.71	115.64	129.87	192.83	0.23	3.5	6.39e-06
Fenrir	2.26	1.26	145.74	70.69	90.15	13.51	0.05	2	2.83e-06
Surtur	2.23	3.67	151.56	69.51	273.61	278.60	0.15	3	6.41e-06
Ymir	2.32	3.59	147.38	52.45	10.49	50.08	3.97	9	5.66e-05
Loge	2.28	1.68	165.50	34.68	205.41	155.61	0.15	3	6.34e-06
Fornjot	2.51	1.51	155.28	66.13	252.19	151.99	0.15	3	6.03e-06
S/2007 S2	1.60	2.46	149.23	35.98	120.61	164.29	0.05	2	7.65e-06
S/2004 S13	1.84	2.97	144.12	59.43	337.54	218.11	0.15	3	7.11e-06
S/2004 S17	1.93	2.09	159.87	17.13	312.76	212.59	0.05	2	3.07e-06
S/2006 S1	1.88	0.94	177.45	336.83	338.38	232.92	0.15	2.5	7.01e-06
S/2004 S12	1.99	3.76	166.32	64.22	238.57	255.30	0.09	2.5	6.81e-06
S/2004 S7	2.02	4.95	167.05	26.09	283.95	189.70	0.15	3	6.75e-06
S/2007 S3	1.92	1.97	149.95	35.58	2.52	55.99	0.09	2.5	6.96e-06
S/2006 S3	2.11	4.78	132.05	71.61	177.71	165.68	0.15	2.5	6.60e-06

Sources: Yeomans (2006) e Sheppard (2019)

Table A.3: Orbital elements, physical parameters, and dust production of the group's satellites with a radius greater than 100 km. The values were obtained by the Horizons system, referring to July 16, 2019.

Satellites	a ($\times 10^5$) (km)	e ($\times 10^{-2}$)	I (°)	Ω (°)	ω (°)	f (°)	m ($\times 10^{19}$) (kg)	R (km)	M^+ (kg/s)
Mimas	1.86	1.70	1.57	241.36	203.44	199.08	3.75	198.8	5.03e-01
Enceladus	2.38	0.62	0.01	259.30	154.66	331.29	10.80	252.3	6.75e-01
Tethys	2.95	0.09	1.09	288.00	193.35	353.80	61.76	536.3	2.62e+00
Dione	3.78	0.19	0.02	59.89	52.34	112.40	109.57	562.5	2.43e+00
Rhea	5.27	0.11	0.33	160.65	48.72	31.191	230.9	764.5	3.58e+00
Titan	12.22	2.87	0.41	250.36	323.53	330.09	13455.3	2575.5	2.39e+01
Hyperion	14.86	13.09	1.03	229.79	355.84	195.38	1.08	133	5.66e-02
Iapetus	35.60	2.84	15.77	253.46	348.78	187.84	180.59	734.5	1.04e+00

Source: Yeomans (2006)

Table A.4: Orbital elements, physical parameters, and dust production of the new moons discovered around Saturn in 2019. The values were obtained by the Horizons system, referring to July 16, 2019, and from Sheppard (2019).

Satellites	a ($\times 10^7$) (km)	e ($\times 10^{-1}$)	I (°)	Ω (°)	ω (°)	f (°)	m ($\times 10^{15}$) (kg)	R (km)	M^+ (kg/s)
S/2004 S20	1.92	2.08	169.39	36.97	1.26	161.04	0.05	2	1.23e-05
S/2004 S21	2.27	3.22	130.37	22.31	243.75	267.55	0.15	1.5	1.13e-05
S/2004 S22	2.08	2.41	152.75	45.54	346.67	235.17	0.15	1.5	1.18e-05
S/2004 S23	2.11	3.71	150.06	44.85	82.48	95.57	0.05	1.5	1.17e-05
S/2004 S24	2.29	0.84	62.966	209.87	36.67	194.45	0.05	1.5	1.12e-05
S/2004 S25	2.09	4.42	153.19	55.07	235.52	237.19	0.03	1.5	6.64e-06
S/2004 S26	2.64	1.53	160.52	37.78	322.35	302.82	0.05	2	1.04e-05
S/2004 S27	2.02	1.11	145.50	19.92	205.91	190.90	0.05	2	6.76e-06
S/2004 S28	2.18	1.36	142.51	36.12	235.87	48.46	0.03	2	6.49e-06
S/2004 S29	1.69	4.39	23.900	342.27	13.07	45.47	0.05	2	1.32e-05
S/2004 S30	2.06	1.26	148.89	86.19	208.83	135.03	0.05	1.5	1.19e-05
S/2004 S31	1.75	2.38	57.012	282.95	281.49	0.15	0.03	2	7.28e-06
S/2004 S32	2.10	2.65	163.84	88.51	334.98	191.91	0.05	2	1.18e-05
S/2004 S33	2.43	3.91	141.43	9.13	19.54	188.50	0.03	2	6.13e-06
S/2004 S34	2.41	2.30	161.13	66.96	263.01	40.68	0.03	1.5	6.16e-06
S/2004 S35	2.220	1.85	155.07	42.08	46.28	224.36	0.05	2	1.14e-05
S/2004 S36	2.34	7.40	135.65	72.67	191.73	197.71	0.03	1.5	2.78e-06
S/2004 S37	1.60	4.97	134.97	38.90	115.70	293.68	0.03	2	1.36e-05
S/2004 S38	2.21	4.42	127.46	26.52	26.80	335.16	0.05	2	1.15e-05
S/2004 S39	2.37	0.69	139.56	49.13	202.61	230.30	0.03	1	6.21e-06

Source: Yeomans (2006) e Sheppard (2019)

Table A.5: Orbital elements, physical parameters, and dust production of the new moons discovered between 2019 and 2021. The values were obtained by the Horizons system, referring to July 16, 2019, and from Sheppard (2019).

Satellites	a ($\times 10^7$) (km)	e ($\times 10^{-1}$)	I (°)	Ω (°)	ω (°)	f (°)	m ($\times 10^{15}$) (kg)	R (km)	M^+ (kg/s)
S/2020 S1	1.14	0	47.01	0	0	0	0	1	1.02e-06
S/2006 S9	1.45	0	174.10	0	0	0	0	1	8.95e-07
S/2004 S40	1.62	0	169.80	0	0	0	0	1	8.44e-07
S/2019 S2	1.66	0	176.10	0	0	0	0	1	8.32e-07
S/2019 S3	1.72	0	164.20	0	0	0	0	1	8.18e-07
S/2020 S2	1.75	0	170.50	0	0	0	0	1	7.95e-07
S/2007 S5	1.81	0	184.00	0	0	0	0	1	8.50e-07
S/2020 S3	1.88	0	193.00	0	0	0	0	1	7.98e-07
S/2019 S4	1.95	0	201.00	0	0	0	0	1	7.98e-07
S/2004 S41	2.03	0	215.00	0	0	0	0	1	7.98e-07
S/2020 S4	2.10	0	221.00	0	0	0	0	1	7.94e-07
S/2020 S5	2.19	0	229.00	0	0	0	0	1	7.87e-07
S/2007 S6	2.28	0	235.00	0	0	0	0	1	7.84e-07
S/2004 S42	2.38	0	248.00	0	0	0	0	1	7.94e-07
S/2006 S10	2.47	0	254.00	0	0	0	0	1	7.78e-07
S/2019 S5	2.56	0	260.00	0	0	0	0	1	7.76e-07
S/2004 S43	2.65	0	270.00	0	0	0	0	1	7.76e-07
S/2004 S44	2.74	0	281.00	0	0	0	0	1	1.72e-06
S/2004 S45	2.83	0	292.00	0	0	0	0	1	1.69e-06
S/2006 S11	2.92	0	303.00	0	0	0	0	1	7.63e-07
S/2006 S12	3.01	0	315.00	0	0	0	0	1	7.56e-07
S/2019 S6	3.10	0	326.00	0	0	0	0	1	7.54e-07
S/2006 S13	3.19	0	338.00	0	0	0	0	1	7.52e-07
S/2019 S7	3.28	0	350.00	0	0	0	0	1	7.44e-07
S/2019 S8	3.37	0	362.00	0	0	0	0	1	7.48e-07
S/2019 S9	3.46	0	374.00	0	0	0	0	1	7.42e-07
S/2004 S46	3.55	0	387.00	0	0	0	0	1	7.49e-07
S/2019 S10	3.64	0	400.00	0	0	0	0	1	7.36e-07
S/2004 S47	3.73	0	412.00	0	0	0	0	1	8.48e-07
S/2019 S11	3.82	0	424.00	0	0	0	0	1	7.44e-07
S/2006 S14	3.91	0	437.00	0	0	0	0	1	7.31e-07
S/2019 S12	4.00	0	450.00	0	0	0	0	1	7.36e-07

Continues on next page

Table A.5 — continued from previous page

Satellites	a ($\times 10^7$) (km)	e ($\times 10^{-1}$)	I ($^\circ$)	Ω ($^\circ$)	ω ($^\circ$)	f ($^\circ$)	m ($\times 10^{15}$) (kg)	R (km)	M^+ (kg/s)
S/2020 S6	4.09	0	463.00	0	0	0	0	1	7.32e-07
S/2019 S13	4.18	0	475.00	0	0	0	0	1	7.35e-07
S/2005 S4	4.27	0	487.00	0	0	0	0	1	4.08e-06
S/2007 S7	4.36	0	500.00	0	0	0	0	1	8.53e-07
S/2007 S8	4.45	0	513.00	0	0	0	0	1	8.21e-07
S/2020 S7	4.54	0	526.00	0	0	0	0	1	8.15e-07
S/2019 S14	4.63	0	540.00	0	0	0	0	1	7.96e-07
S/2019 S15	4.72	0	553.00	0	0	0	0	1	7.30e-07
S/2005 S5	4.81	0	566.00	0	0	0	0	1	7.34e-07
S/2006 S15	4.90	0	579.00	0	0	0	0	1	7.24e-07
S/2006 S16	4.99	0	592.00	0	0	0	0	1	7.17e-07
S/2006 S17	5.08	0	605.00	0	0	0	0	1	1.59e-06
S/2004 S48	5.17	0	618.00	0	0	0	0	1	1.60e-06
S/2020 S8	5.26	0	631.00	0	0	0	0	1	7.20e-07
S/2004 S49	5.35	0	644.00	0	0	0	0	1	7.03e-07
S/2004 S50	5.44	0	657.00	0	0	0	0	1	7.17e-07
S/2006 S18	5.53	0	670.00	0	0	0	0	1	1.56e-06
S/2019 S16	5.62	0	683.00	0	0	0	0	1	6.90e-07
S/2019 S17	5.71	0	696.00	0	0	0	0	1	1.57e-06
S/2019 S18	5.80	0	709.00	0	0	0	0	1	6.92e-07
S/2019 S19	5.89	0	722.00	0	0	0	0	1	6.93e-07
S/2019 S20	5.98	0	735.00	0	0	0	0	1	6.93e-07
S/2006 S19	6.07	0	748.00	0	0	0	0	1	6.97e-07
S/2004 S51	6.16	0	761.00	0	0	0	0	1	1.48e-06
S/2020 S9	6.25	0	774.00	0	0	0	0	1	6.57e-07
S/2004 S52	6.34	0	787.00	0	0	0	0	1	6.56e-07
S/2007 S9	6.43	0	800.00	0	0	0	0	1	7.43e-07
S/2004 S53	6.52	0	813.00	0	0	0	0	1	6.88e-07
S/2020 S10	6.61	0	826.00	0	0	0	0	1	6.70e-07
S/2019 S21	6.70	0	839.00	0	0	0	0	1	6.56e-07
S/2006 S20	3.41	0	492.00	0	0	0	0	1	2.12e-06

Source: Yeomans (2006) and Sheppard (2019)